Laminin-defined Mechanical Status Modulates Retinal Pigment Epithelium Functionality

Aleksandra N. Kozyrina*[1, 2], Teodora Piskova*[1, 2], Francesca Semeraro[1, 2], Iris C. Doolaar[3,4], Taspia Prapty[1, 2], Tamás Haraszti[3, 4], Maxime Hubert[5, 6], Reinhard Windoffer[2], Rudolf E. Leube[2], Ana-Sunčana Smith[5, 6] and Jacopo Di Russo[1, 2, 3]

* equal contribution

1. Interdisciplinary Centre for Clinical Research, RWTH Aachen University, Pauwelstrasse 30, 52074 Aachen, Germany.
2. Institute of Molecular and Cellular Anatomy, RWTH Aachen University, Wendlingweg 2, 52074 Aachen, Germany.
3. DWI – Leibniz-Institute for Interactive Materials, Forckenbeckstrasse 50, 52074 Aachen, Germany.
4. Institute for Technical and Macromolecular Chemistry, RWTH Aachen University, Worringerweg 1-2, Aachen D-52074, Germany.
5. PULS Group, Department of Physics and Interdisciplinary Center for Nanostructured Films, Friedrich-Alexander University of Erlangen-Nürnberg, 91058 Erlangen, Germany.
6. Group for Computational Life Sciences, Division of Physical Chemistry, Rudjer Bošković Institute,10000 Zagreb, Croatia.

Correspondence:

Jacopo Di Russo

jdirusso@ukaachen.de

ABSTRACT

Epithelial cells are highly interconnected, whereby they acquire mesoscale mechanical properties to accomplish specific tissue functions. In homeostasis, this mechanical status can be summarised as mechanical homeostasis, regulated by the balance of intercellular tension and extracellular matrix adhesion forces. In the outer retina, the significance of this force balance and its consequences for vision remains poorly understood. The retinal pigmented epithelium (RPE) is located at the base of the retina and supports vision by ensuring the light sensitivity and lifespan of photoreceptor cells. Given the varying photoreceptor densities along the visual angle, the functional demand on the RPE varies from the most illuminated macula to the retinal periphery and corresponds to a significant difference in RPE homeostatic state. In this work, we hypothesised that extracellular matrix (ECM) cues define the relation between RPE mechanical status and functional capacity. We found that the density of basement membrane laminins modulates the level of RPE contractility, which directly controls the efficiency of the epithelium in phagocytosing photoreceptor outer segments. *In vivo*, the density gradient of laminin α5 and 332 follows retinal functional demand, supporting the physiological role of laminins in controlling RPE mechanical homeostasis. Our data suggest that laminin density and isoforms can differentially engage integrins β1 and β4, the ratio of which determines the contribution of actin vs keratin cytoskeleton in balancing tissue mechanics. With this work, we suggest that the ECM-defined mechanical status of RPE is a novel parameter for visual function, opening new paths of investigation and treatment for sight-threatening diseases such as high myopia and age-related macular degeneration.

The mechanical properties of any tissue define its function and state [1,2]. In a homeostatic state, these mechanical features are maintained in a preferred range for optimal activity, also known as tissue mechanical homeostasis [3]. One of the main players in defining the mechanical homeostasis of tissues is its extracellular matrix (ECM) composition [4,5].

In the retina, the most prominent ECM structure is the Bruch's membrane, situated at its outermost part, also known as outer retina [6]. The Bruch's membrane favours nutrient exchange between the choroid vessels and the retina and distally provides structural support and adhesion to the retinal pigment epithelium (RPE). The RPE is a postmitotic cell monolayer which directly interfaces with the light-detecting neural tissue. In the developing eye, the RPE organises the retina [7,8], while in the adult, it plays a key role in the visual cycle [9,10]. One of the main activities of RPE cells is the daily phagocytosis of shed photoreceptor cell fragments, therefore mediating the constant renewal of their light-sensitive outer segments and ensuring photoreceptor lifespan and light sensitivity [11–13]. The number of photoreceptor outer segments (POS) per RPE cell is not constant within the eye, with an average of 25-30 POS per RPE cell in the central and macular area and decreasing towards the periphery (~ 15 POS) [14], indicating a gradient of functional demand.

RPE cells are polygonal in shape and tightly adhere to each other: they arrange as a honeycomb-like structure in the centre, which gradually shifts to a more elongated and less organised structure towards the retinal periphery, which suggests a change in its mechanical status [15–17].

Although the Bruch's membrane is known to spatially vary along the visual axis [6], it remains an open question how this influences RPE mechanical homeostasis. Here, we hypothesise that the spatial variation of Bruch's membrane cues controls RPE mechanical status and region-dependent functional capacity.

In this work, we find that the relative density of laminin 511 and 332 defines the level of RPE contractility, which directly controls its functional capacity. At low density, laminin 511 promotes high contractility in RPE, which differs from laminin 332 due to a lower integrin β4 vs β1 engagement. In vivo, we find that the density gradient of these laminin isoforms corresponds to changes in RPE mechanical status and functional demand.

These findings for the first time underline the importance of mechanical homeostasis in RPE and, in general, in the outer retina. The significance of RPE mechanical status for visual function in adults opens the question of its role in ageing and sight-threatening diseases such as (high) myopia and age-related macular degeneration. Finally, this study could incentivize a larger use of Rho kinase inhibitors, currently used as anti-glaucoma medications, for other retinal diseases.

RESULTS

Mechanical status of the RPE correlates with biochemical heterogeneity of Bruch's membrane.

To understand the possible relation between RPE mechanical status and Bruch's membrane biochemical and mechanical cues, we characterised the outer retina of adult BALB/C mice (25-30 weeks) (Fig 1). Bruch's membrane, retinal complexity and function have been described in relation to the visual axis [14,17]. In both mice and humans, the central region (macula in humans) exhibits the highest density of photoreceptor cells and the highest photoreceptor to RPE ratio. This ratio gradually decreases with the visual axis, signifying a reduction in RPE functional demand [14]. Hence, we identified three regions with respect to the radial distance from the optic nerve: centre (300-1200 μm), mid periphery (1200-2000 μm) and far periphery (2000-3000 μm) (Fig. 1 A). We observed substantial difference in the organisation of RPE cells along the radial distance (Fig. 1 A), consistent with previous reports [15–17]. From a classic honeycomb arrangement in the centre, the RPE gradually changes to a monolayer consisting of more elongated cells at the far periphery (Fig. 1 A; sup fig. 1 A, D) [15–17].

The topology and morphology of an epithelial monolayer define its mechanical properties [18–20]. Hence, we performed morphometric characterisation of RPE cells in the different regions of the retina (Fig.1 B - D, sup. fig. 1 A - H). RPE cells have the largest area and perimeter in the central region ($\langle A \rangle$ = 469 μm^2; $\langle P \rangle$ = 84 μm), whereas they become smaller towards the mid periphery ($\langle A \rangle$ = 349 μm^2; $\langle P \rangle$ = 74 μm) and far periphery ($\langle A \rangle$ = 343 μm^2; $\langle P \rangle$ = 75 μm) (Sup. fig.1 F, G). Next, to better quantify the mechanics of this differential cell arrangement, we calculated the shape factor for each cell, defined as the cell perimeter P divided by the square root of the corresponding cell area A. This density-independent shape factor has been theorised to describe epithelial rigidity based on the balance between cortical tension and cell-cell adhesion energy, with lower values where the first element is more prominent [21]. Our data show an average value in the retinal central region of 3.8, which gradually increases till reaching values over 4.0 at the far periphery. This implies a gradual increase of intercellular tension, coinciding with the decreasing RPE functional demand (Fig. 1 B, C, sup. fig. 1 E) [14]. Additionally, the comparison of the cellular nuclear geometry shows a reduced roundness and circularity corresponding to a higher aspect ratio towards the far periphery, supporting the existence of different levels of intracellular strain (sup. fig. 1 I - K). Finally, we noticed the presence of two distinct cell populations in the centre and mid periphery, visible when cell area and cell perimeter distributions are normalised and compared (Fig. 1 D, sup. fig. 1 H). Hence, we compared the topological relations of RPE cells across retinal regions by plotting the rescaled cell areas and perimeters as a function of the number of neighbours (respectively Lewis' law [22–25] and Desh's law [26]) (Fig. 1 E, sup. fig. 1 M). Both comparisons show different curve behaviour in the retinal regions, especially evident between the centre and far periphery.

To gain further insight into monolayer topology, we then correlated the number of neighbours *n* of each cell and the average number of neighbours *m(n)* of any adjacent cells to the first with *n* sides (Aboav-Weaire's laws) (Fig. 1 F) [27–29]. This relation describes the mean number of neighbours that neighbouring cells have via the topological parameter *b(n)* (see method section). The different regions show a linear relationship, as in any functional epithelium [20,27–29]. Nevertheless, a shift is visible between values, suggesting a topological variation of RPE from the centre to the far periphery (Fig. 1 F, sup. fig. L). Altogether, the extensive image-based morphometric and topological analyses (of more than 5500 cells from three mice – see method section) strongly support the existence of different mechanical status in the monolayer from the retinal central region to the far periphery.

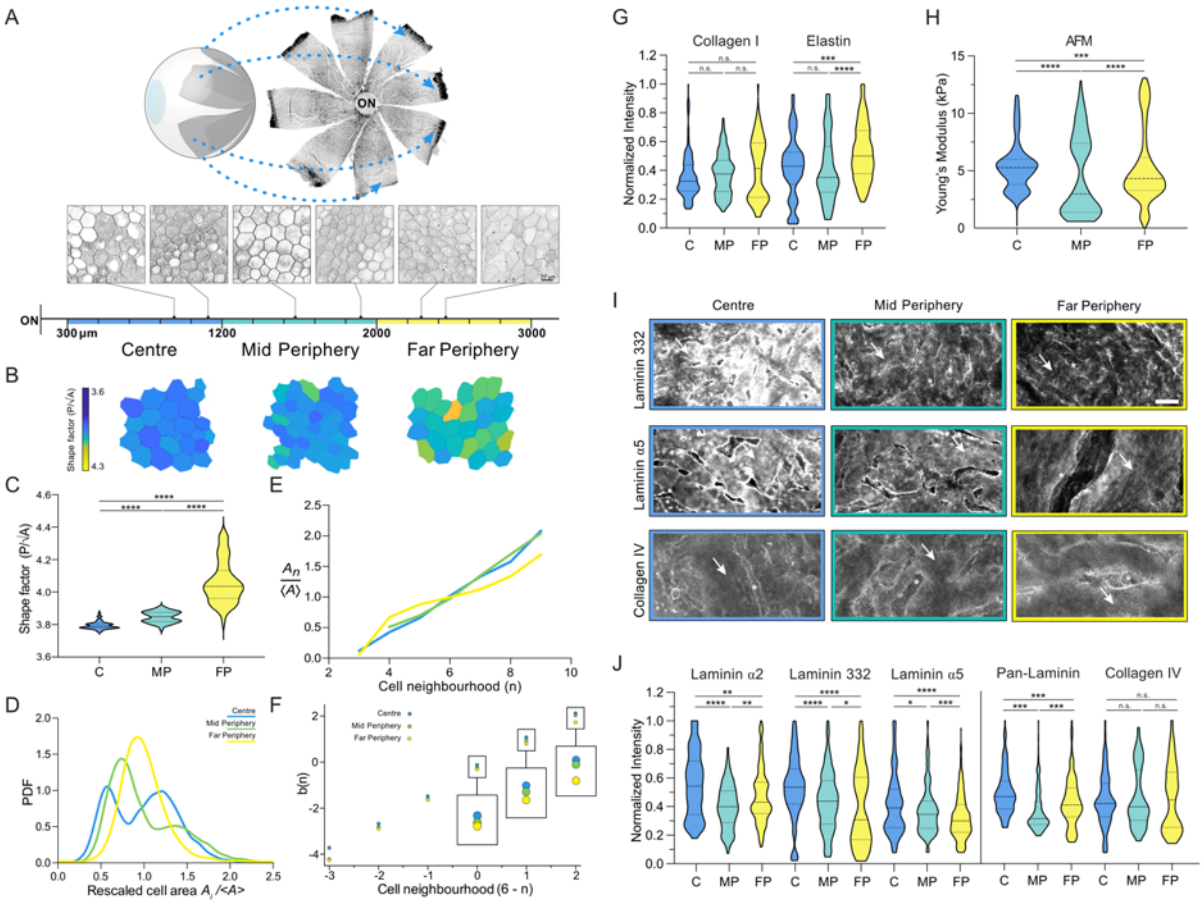

Figure 1: Spatial heterogeneity of murine retinal pigment epithelium topology and Bruch's membrane composition. ***(A)*** *Murine retina flat mount indicating the regions used for analyses and representative F-actin staining of RPE. The regions were defined by the distance from the optic nerve head: centre (300 – 1200 µm), mid periphery (1200 – 2000 µm) and far periphery (2000 – 3000 µm).* ***(B)*** *Representative cell shape index maps for the three regions. The shape index is identified as the perimeter divided by the square root of the area for each cell.* ***(C)*** *Violin plot of mean RPE shape factors from the different regions of the eye analysed from 7 mice.* ***(D)*** *The probability density function (PDF) of the rescaled cell areas defined by $A_i/\langle A\rangle$, A_i being the individual cell area and $\langle A\rangle$ being the average cell area within a given image. More than 5500 cells were analysed from 3 mice.* ***(E)*** *Lewis' law representing the relationship between rescaled cell area and neighbourhood varying for three different regions from 3 mice.* ***(F)*** *Aboav-Weaire's laws showing the variation of the topological parameter b(n) depending on the number of neighbours for each neighbouring cell between different retinal regions from 3 mice.* ***(G)*** *Violin plots of mean fluorescence intensity of interstitial matrix components of the Bruch's membrane. Data were collected from 3 mice and normalized to the highest intensity per mouse.* ***(H)*** *Violin plots of the regional Young's modulus of the Bruch's membrane from 5 mice.* ***(I)*** *Representative immunofluorescent images of the Bruch's membrane stained for laminin 332, laminin α5 and collagen type IV. Arrows and stars indicate RPE basement membrane surface and preparation artefacts respectively. Scale bar 20 µm.* ***(J)*** *Violin plots of mean fluorescence intensity of basement membrane components: laminin α2, laminin 332, laminin α5, pan-laminin, and collagen type IV. Each region contains the quantification of at least 7 sectors from a minimum of 3 to 6 mice. The data were statistically tested with Mann-Whitney test: *p < 0.05; ** p < 0.01; *** p < 0.001; **** p < 0.0001; n.s. = not significant.*

Next, we quantified the distribution of mechanical and biochemical cues within the Bruch's membrane. In the epithelial ECM, mechanical cues are mostly determined by the composition and crosslinking density of the interstitial matrix [5]. Therefore, we used confocal microscopy and immunofluorescence staining to quantify the amount of collagen type I and elastin present in the Bruch's membrane. The average fluorescence intensity quantification of the retina's central, mid peripheral, and far peripheral regions are comparable with the data reported in the literature [30,31] (Fig. 1 G). Furthermore, we measured the Young's modulus of the Bruch's membrane in different regions using atomic force microscopy (AFM) and indenting into the decellularised ECM by ~ 200 nm. The quantification resulted in a highly variable distribution of the data, with the centre having the most frequent (mode) stiffness of 5.5 kPa, the mid periphery 1.5 kPa and the far periphery 4 kPa (Fig. 1 H). This biphasic stiffness trend suggests that ECM mechanical cues may not be the primary factor governing RPE mechanical homeostasis concerning functional demand.

From the biochemical point of view, the basement membrane provides cues to epithelia regulating its homeostasis with a key role of the different laminin isoforms [5]. Thus, we characterised the composition and relative amount of the main basement membrane components in the Bruch's membrane, namely laminins and collagen type IV (Fig. 1 I, J). Notably, we detected a significant difference in the amount of laminin isoforms along the visual axis, whereas collagen type IV remained unchanged. This supports the idea of the importance of laminins in the differential biochemical signalling to the RPE. Among the laminin isoforms detected in Bruch's membrane, we noticed a biphasic trend for laminin α2-containing isoforms, with higher (fluorescence) intensity in the centre and far periphery and lower in the mid periphery. Laminin 332 and isoforms containing laminin α5 had the highest (fluorescence) intensity in

102 the centre that gradually diminished towards the periphery (Fig. 1 I, J), following photoreceptor
103 density and functional demand. No laminin α1- or α4-containing isoforms were detected.
104 Altogether, the characterisation of the murine outer retina suggests a possible relationship between
105 the relative density of Bruch's membrane's laminins and region-dependent RPE mechanical status.
106
107 **Laminin 511 density influences contractility levels in RPE monolayers.**
108 The characterization of RPE cell topology and morphology in the retina suggested a relationship
109 between laminin density in the basement membrane and monolayer mechanical status. To dissect the
110 nature of this relationship, we established a bottom-up approach to scrutinize the role of the specific
111 laminin isoforms and their density gradient. Human induced pluripotent stem cell-derived RPE (hiPSC-
112 RPE) cells have already been successfully employed to model mature RPE and to study their
113 functionality [32,33]. Hence, we used hiPSC-RPE cells to obtain monolayers on polyacrylamide (PAA)
114 hydrogels with 4 kPa Young's modulus to best mimic Bruch's membrane stiffness. hiPSC-RPE cells
115 adhere and form a mature monolayer when seeded on PAA gels coated with different concentrations
116 of laminin 511 (composed by laminin α5, β1 and γ1) and laminin 332, both in combination with collagen
117 type IV (Sup. fig. 2 A). After a week of culture, hiPSC-RPE cells reach a low proliferative state (less than
118 8% in 24h) and form a thick polarised monolayer (~10 - 15 μm at the junctions), presenting apical
119 microvilli as shown by ezrin staining and scanning electron microscopy (Fig. 2 A – D, sup. fig. 2 B). The
120 gels were functionalised according to the method described in Przybyla et al. [34] with specific
121 concentrations of laminin, reaching saturation at a coating concentration of around 20 μg/ml (Sup fig.
122 2 C). The advantages of PAA gel as a culture substrate are its defined stiffness (Youngs's modulus of
123 the gel) and the protein-repellent nature of the polymer [35], allowing control over the biochemical cues
124 originating from the coating. In fact, the staining for fibronectin confirmed the absence of aberrant
125 deposition of ECM proteins by the cells while cultured (Sup. fig. 2 D). Due to this reductionistic
126 approach, certain coating conditions were not permissive to obtain mature and intact RPE monolayers,
127 such as laminin 511 and collagen type IV alone or laminin 211 (composed by laminin α2, β1 and γ1)
128 also in combination with collagen type IV (Sup. fig. 2 A, E and F). In conclusion, this reductionistic
129 approach suggests that mainly laminin 511 and 332, but not laminin 211, support RPE adhesion *in*
130 *vivo*.
131 Next, following the logic of a comparative approach between *in vivo* and *in vitro* systems, we
132 performed morphometric and topological analyses of the monolayers obtained on the different laminin
133 isoforms and densities (Fig. 2 E - G, sup. fig. 3 A - C). The calculation of the average cellular area,
134 perimeter, elongation and neighbourhood revealed a stable relationship among all laminin densities
135 and isoforms, excluding their direct role in controlling monolayer morphology and topology.

136 Nevertheless, we wondered if those laminin coatings may affect contractile forces of the monolayer.
137 We used traction force and monolayer stress microscopy to quantify RPE cell-matrix traction forces
138 and cell-cell stresses in different conditions (Fig. 2 H - K). The quantifications revealed an overall ability
139 of laminin 511 to promote higher traction forces compared to laminin 332 (Fig. 2 H, I), with the largest
140 difference recorded at the lowest laminin density (170 Pa vs 80 Pa at 5 µg/ml) (Fig. 2 I). Next, we used
141 the information on the traction forces and monolayer height (Sup. fig. 2 B) to calculate intercellular
142 normal stresses in the different conditions as previously shown [36,37] (Fig. 3 H, J and K). Similarly, we
143 observed a significant difference in the overall monolayer absolute stresses at the lowest coating
144 density of laminins (5 µg/ml) with an average of ~1 Pa for laminin 511 and 0.6 Pa for laminin 332 (Fig.
145 2 K). As expected, the stress vectors exhibit an average close to 0 Pa for both coatings and densities,
146 indicating that monolayers are nearly in equilibrium despite the variations in absolute contractility (Fig.
147 2 J). The difference in traction and stress at the lowest laminin 511 density hypothetically might be
148 caused by a gradual increase in cell adhesion to collagen type IV, which remained constant across the
149 conditions. We therefore tested the effect of collagen type IV on monolayer traction forces using
150 laminin 332 as a control since laminin 511 alone does not support the formation of a monolayer (Sup.
151 fig. 2 E). The quantification shows an overall decrease (~ 40%) of traction in the presence of collagen
152 type IV (Sup. fig. 3 D), excluding the role of collagen type IV for the observed increased traction at the
153 lowest laminin 511 density. Moreover, the clear distinction in traction between laminin 511 and laminin
154 332 strengthens the conclusion that the observed changes are exclusively laminin-induced.
155 Finally, we wanted to understand if the coating density could generally impact RPE cell surface
156 stiffness, which may regulate its apical interaction with the neural retina. Therefore, we performed
157 nanoindentation of RPE cells within the monolayers using a spherical probe of approximately 10 µm
158 radius and quantified the average Effective Young's modulus of the monolayers (Fig. 2 L). The data
159 show that RPE monolayers on laminin 511 are stiffer (~1.5 kPa) compared to laminin 332 (~1 kPa)
160 regardless of the protein surface density.
161 Altogether, the biomechanical characterisation of our model clearly indicates a divergent effect of the
162 low density of laminin 511 versus laminin 332 on the overall RPE mechanical balance, promoting an
163 increased contractility of the monolayer on laminin 511.

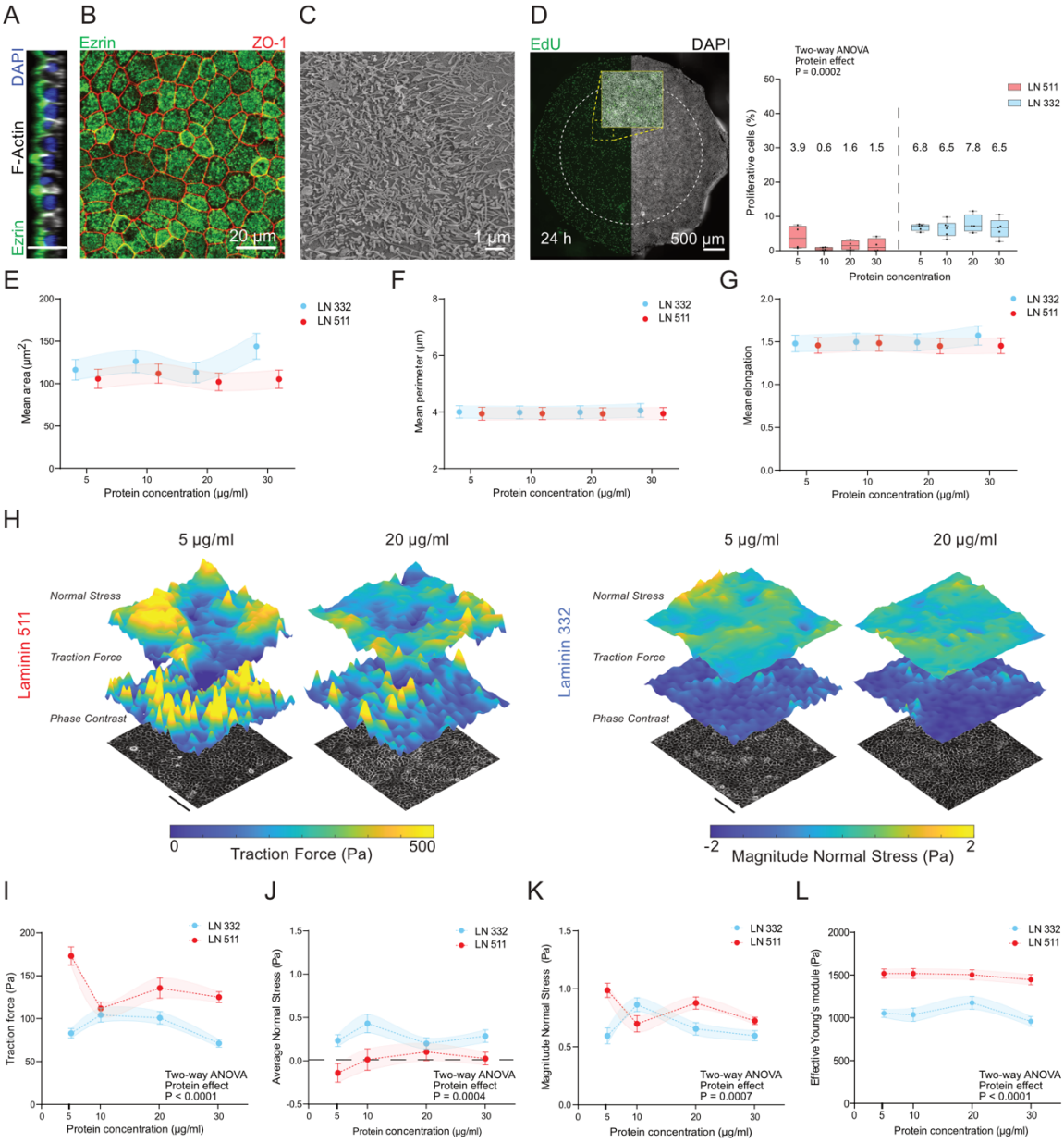

164

Figure 2: Reductionistic approach reveals the effect of laminin density on RPE biomechanics. *hiPSC-derived RPE obtained on PAA gel with Young's modulus of 4 kPa coated with laminin 511 or laminin 332 in the presence of collagen type IV. After one week in culture, cells form a polarized monolayer as observed in a confocal cross-section stained for the microvilli marker Ezrin* ***(A),*** *mature tight junctions (ZO-1)* ***(B),*** *and distinct apical microvilli as observed in the scanning electron micrograph of the monolayer surface* ***(C)****. DAPI staining marks the nuclei.* ***(D)*** *Cellular proliferation rate within 24 h obtained using EdU labelling assay for cells cultured on the PAA gel surface. A representative picture of the gel overview indicates the number of proliferating cells within one gel (left). The ratio of nuclei with incorporated EdU (per cent of proliferative cells) was quantified by the fluorescent signal in the central region of the gel to avoid possible edge effects (white circle). The data show average values ± SEM from at least 4 independent experiments. Statistic was performed using a mixed-effects model (REML) with the Geisser-Greenhouse correction, Tuckey's multiple comparisons test. Morphometric analyses of the cells reveal the absence of significant difference in cellular mean area* ***(E)****, mean perimeter* ***(F)*** *and mean elongation* ***(G)*** *between different laminin isoforms and densities from 3 independent experiments.* ***(H)*** *Representative traction force and monolayer stress profiles for different coating conditions and their quantifications* ***(I, J and K)*** *show a significant increase in contractility of RPE monolayers at the lowest laminin 511 density.* ***(L)*** *Quantification of the effective Young's modulus of the apical side of monolayer in different conditions. Data are shown as average ± SEM from at least 4 independent experiments. Statistical analyses were performed using a mixed-effects model (REML) with the Geisser-Greenhouse correction, Tuckey's multiple comparisons test.*

165

166 **Laminin-defined traction levels modulate RPE efficiency to phagocyte photoreceptor outer**
167 **segments.**
168 Epithelial contractility levels have been shown to directly influence tissue functionality and reactivity [36–
169 43]. Therefore, considering the difference in RPE mechanics on lower laminin density, we wondered if
170 there is any direct relationship between the monolayer status and its functional capacity. To understand
171 this, we tested the ability of RPE monolayers on PAA gels to perform their fundamental physiological
172 function: to bind and phagocyte POS fragments, which were isolated from porcine eyes and
173 fluorescently labelled with FITC (Fig. 3 A - C). The quantification shows that, overall, at high laminin
174 coating density (10 - 30 µg/ml) there is a comparable efficiency of phagocytosis between laminin 332
175 and 511, whereas a divergence could be detected at the coating density of 5 µg/ml with reduced
176 efficiency of RPE on laminin 511 (~50 %) (Fig. 3 B, C). These results highly correlate with the traction
177 force levels in RPE monolayers, suggesting a cause-effect relation between laminin-defined traction
178 and RPE functional capacity. Hence, we addressed whether the efficiency of POS phagocytosis is
179 directly affected by the level of RPE traction forces independently of the biochemical nature of ECM
180 adhesion (i.e., laminin isoforms or density) (Fig. 3 D - J).
181 To systematically adjust the traction force, we decided to tune either the ECM physical cues (i.e.,
182 hydrogel stiffness) or the biochemical nature of adhesion (i.e., laminins vs vitronectin) (Fig. 3 D). We
183 then assessed the RPE efficiency in internalising POS by comparing it with the maximum efficiency
184 observed in RPE on laminins. First, we obtained RPE monolayers on stiffer hydrogels (18 kPa) coated
185 with laminin 511 or 332 (20 µg/ml) in the presence of collagen type IV (30 µg/ml), which developed a
186 significantly increased traction force compared to the one on 4kPa (~140 Pa for 511 and ~170 Pa for
187 332). This corresponded to a reduced efficiency of these monolayers for POS internalisation (~ 40%)
188 (Fig. 3 E - G). Second, we measured the phagocytic activity and traction forces of monolayers obtained
189 on 4 kPa hydrogels coated with a high concentration of vitronectin (250 µg/ml) to match the protein
190 surface density of laminins. Also in this case, the analyses revealed a higher average traction force
191 (~ 200 Pa) which corresponded to a reduced ability of RPE to internalise POS (~ 36%) (Fig. 3 E – G).
192 To distinguish the exclusive role of cellular contractility from the possible converging effects of ECM
193 signalling, we inhibited or increased actomyosin contractility in RPE monolayers using a ROCK inhibitor
194 or a RhoA activator (Fig. 3 H - J). The reduction of contractility was performed on RPE monolayers
195 cultured on soft (4 kPa) surfaces coated with collagen type IV (30 µg/ml) with little addition of laminins
196 (2.5 µg/ml) which showed *per se* a low activity for POS phagocytosis (~ 50%). On the other hand, the
197 increase of contractility was induced in RPE on high-density laminins (20 µg/ml) in the presence of
198 collagen type IV. As expected, the drug treatments affected the ability of RPE to develop traction
199 forces with reduced traction after ROCK inhibitor treatment and increased after RhoA activation (Fig.

3 H, J). Moreover, the quantification revealed a direct connection between actomyosin contractility and monolayer efficiency in POS phagocytosis. Independently of the laminin type, RPE phagocytic efficiency increased after ROCK inhibitor treatment (from ~50% to ~70%) and decreased after RhoA activator treatment (from ~70% to ~50%) (Fig. 3 H, J).

Overall, these data demonstrate that low laminin 511 and not 332 density reduces RPE functional capacity by promoting high levels of traction forces.

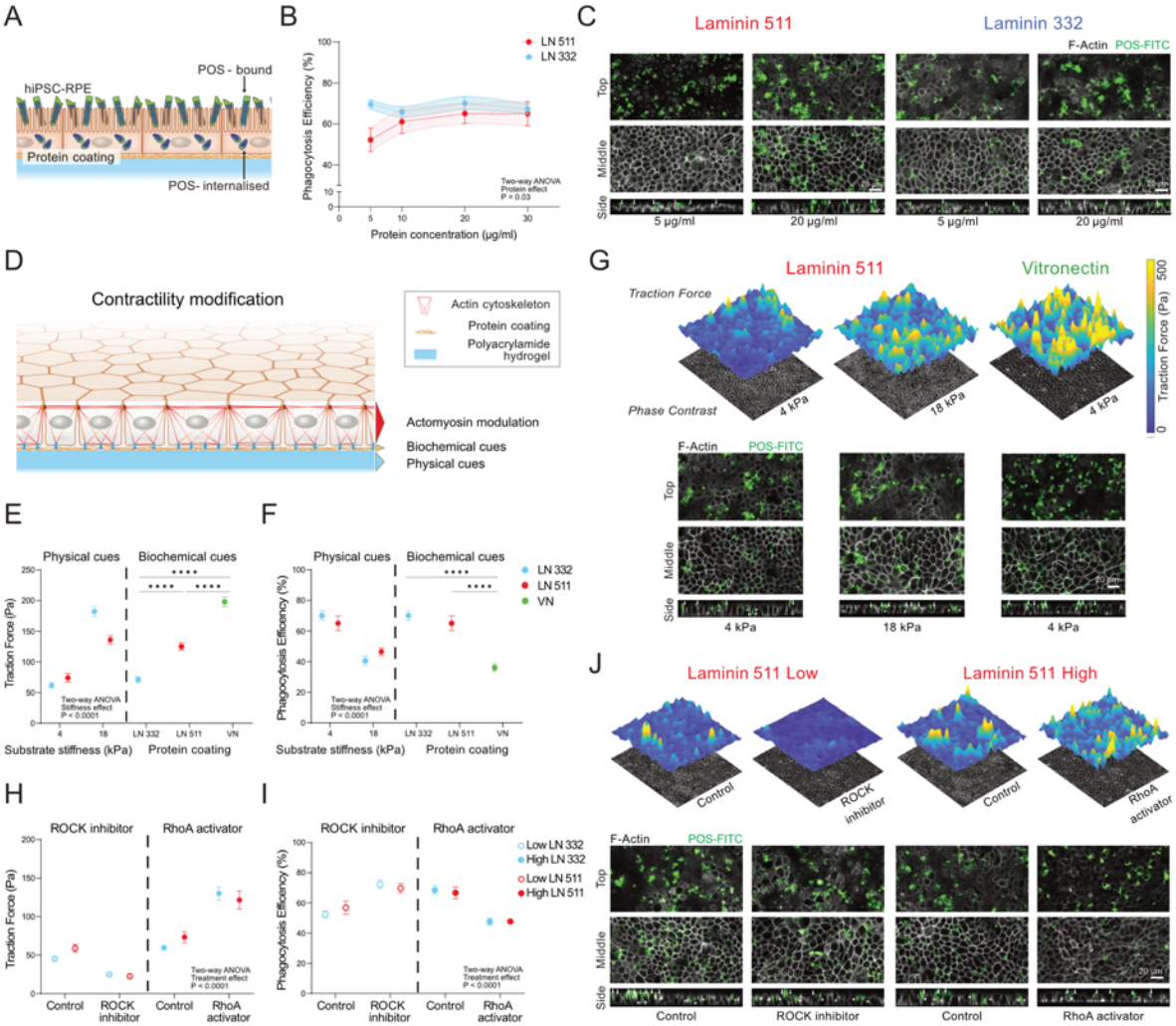

Figure 3: Laminin-defined RPE contractility modulates POS phagocytosis. ***(A)*** *Schematic representation of the photoreceptor outer segment internalisation assay on RPE monolayer.* ***(B)*** *Average phagocytosis efficiency ± SEM for different laminin isoforms and their coating conditions from at least 4 independent experiments. The phagocytosis efficiency is defined as the amount of internalised POS divided by total POS. Statistical significance was tested using a mixed-effects model (REML) with the Geisser-Greenhouse correction, Tuckey's multiple comparisons test.* ***(C)*** *Representative confocal images of the hiPSC-RPE cells on PAA hydrogel with laminin 511 or laminin 332 coating (in the presence of collagen type IV). The top row indicates FITC-labelled POS fragments at the apical surface of the cells. The middle row represents an optical section of the cell monolayer with POS fragments inside. The results of the POS phagocytosis assay are visible in the orthogonal projections (bottom row) where arrows and stars indicate bound and internalised POS respectively.* ***(D)*** *Schematic representation of the experimental strategy to modulate monolayer contractility. Quantification of mean traction forces* ***(E)*** *and phagocytosis efficiency* ***(F)*** *±SEM in RPE upon different ECM physical (stiffness) and biochemical cues (coating). PAA gels were coated with laminin 511 (LN 511) or laminin 332 (LN 332) (in the presence of collagen type IV) or with vitronectin (VN). ****p<0.0001 using mixed-effects model (REML) with the Geisser-Greenhouse correction, Tuckey's multiple comparisons test (physical cues) and Mann-Whitney test (biochemical cues).* ***(G)*** *Representative traction force plots and immunofluorescent images of POS internalisation assay upon different physical or biochemical cues. Drug treatment affecting actomyosin contractility levels using ROCK inhibitor and RhoA activator shows inverse dependence between the level of monolayer contractility (traction forces)* ***(H)*** *and its ability to phagocyte POS fragments* ***(I)****. Data are shown as mean ± SEM. ****p<0.0001 using mixed-effects model (REML) with the Geisser-Greenhouse correction, Tuckey's multiple comparisons paired test.* ***(J)*** *Representative traction force plots and immunofluorescent images of POS internalisation assay upon drug treatment.*

208

209 **Integrin β4/β1 ratio and keratin network organisation modulate RPE mechanical homeostasis along**
210 **the visual axis.**

211 Epithelial cells in homeostasis mechanically couple their cytoskeleton to their basement membrane via
212 integrin receptors [5,44]. Intracellularly, integrin β1 subtypes interface with the actin cytoskeleton via talin,
213 whereas integrin α6β4 binds via plectin the keratin network [45]. Extracellularly, integrins β1 and β4 bind
214 with a redundant number of proteins, including laminins α3 and α5 chains [46,47]. Therefore, we
215 wondered if low densities of laminin 332 or 511 differently promote integrin-based adhesion in RPE,
216 thus influencing traction forces and consequent functional differences. Hence, we performed a
217 functional adhesion assay using blocking antibodies to address the engagement of specific integrin
218 subtypes on laminin-coated hydrogels (Fig. 4 A). Blocking the different beta chains (i.e., β1, β4, and
219 [αv] β3) resulted in a significant reduction of adhesion for β1 (LN 511 ~62% and LN332 ~75%) and no
220 significant effect in the case of β4 and αvβ3 integrins. In the presence of integrin β4 blocking antibody,
221 a tendency of reduction was observed on laminin 332. Hence, to avoid the effect of compensation by
222 β1 integrin, we concurrently blocked integrin β1 and β4, achieving nearly complete inhibition of RPE
223 cell adhesion onto low-density laminin 332 (~94%) with no significant drop on laminin 511 (Fig. 4 A,
224 left). A similar trend was also observed for integrin alpha chains, where a substantial reduction in
225 adhesion occurred upon combining integrin α6- and α3-blocking antibodies, suggesting the
226 predominant involvement of these two subtypes in the adhesion process (Fig. 4 A, right).

227 Based on these findings, we stained target integrins on RPE cells detached from mature monolayers
228 and analysed their relative surface presence during adhesion to the low-density laminin via flow

229 cytometry (Fig. 4 B – E, sup. fig. 4). In line with the adhesion assay, the quantification revealed that
230 cells adhering to the low-density laminin 511 present a significantly higher level of β1 integrin on their
231 surface compared to cells adhering to laminin 332 (Fig. 4 B, C and supp. fig. 4 D). Instead, the levels
232 of β4, α3 and α6 integrins were comparable between low-density laminin 511 and 332 (Fig. 4 D and
233 sup. fig. 4 D - K). Furthermore, these results show that RPE cells adhering to low-density laminin 332
234 present a significantly higher ratio of integrin β4 to β1 compared to cells adhering to low-density
235 laminin 511 (Fig. 4 E). Altogether, these data indicate the main role of integrins α6β1 and α3β1 to
236 support the adhesion to the low-density laminin 511 and integrins α6β1, α3β1, and α6β4 to low-density
237 laminin 332.
238 The formation of hemidesmosomes has been shown to reduce cellular traction forces [48] and sensitivity
239 of nuclear mechanotransduction [49] via their role in nucleation and organization of the keratin
240 cytoskeleton [49,50]. Encouraged by our *in vitro* findings, we were curious whether the different laminin
241 densities in Bruch's membrane coincided with different organisation of the keratin network in RPE.
242 Using keratin 8-YFP knock-in mice[51], we imaged and segmented the keratin network in 3D using a
243 recently developed workflow [52] (Fig. 4 F - J). The analyses revealed that keratin network has thinner
244 filaments (reduced brightness - fig. 4 H), get looser (higher segment length - fig. 4 I) and is more tense
245 (reduced segments curvature - fig. 4 J) from the centre to far periphery.
246 This evidence supports the existence of a laminin-defined mechanical balance in RPE which gradually
247 shifts to a less prominent keratin contribution and more contractile monolayer toward the retinal
248 periphery (Fig. 5).
249

Figure 4 (next page): Laminin density defines RPE mechanical balance via integrin β4/β1 ratio and keratin cytoskeleton organization. (A) *Box and whisker plots of RPE cell adhesion percentage on low-density (5 µg/ml) laminin 332 or laminin 511-coated hydrogels, after incubation with integrin beta or alpha subunits blocking antibodies and control (cntr). * p < 0.05, ** p < 0.01, *** p < 0.001 ****p<0.0001 tested using a two-way ANOVA with Geisser-greenhouse and Tukey correction. Stars standing directly on the box and whisker show significance towards the control.* ***(B)*** *Representative flow cytometry histograms of the surface integrin β1 (top) and β4 (bottom) expression of RPE cell cultured for one week on low-density laminin 332 (light blue), laminin 511 (red), and unstained control (grey).* ***(C, D, E)*** *Box and whisker plots showing the distribution of intensity medians and the relative estimation plots from independent experiments for β1 and β4 integrins and their ratio. * p < 0.05 tested using paired t-test.* ***(F, G)*** *Representative images of RPE cells at different regions from YFP-keratin 8 mice and the resulting cinematic rendering of the keratin network.* ***(H, I, L)*** *Violin plots of normalized keratin brightness, mean segment length, and curvature in RPE from different retinal regions. * p < 0.05, ** p < 0.01 and ****p<0.0001 tested using a one-way ANOVA. Data are from three independent mice.*

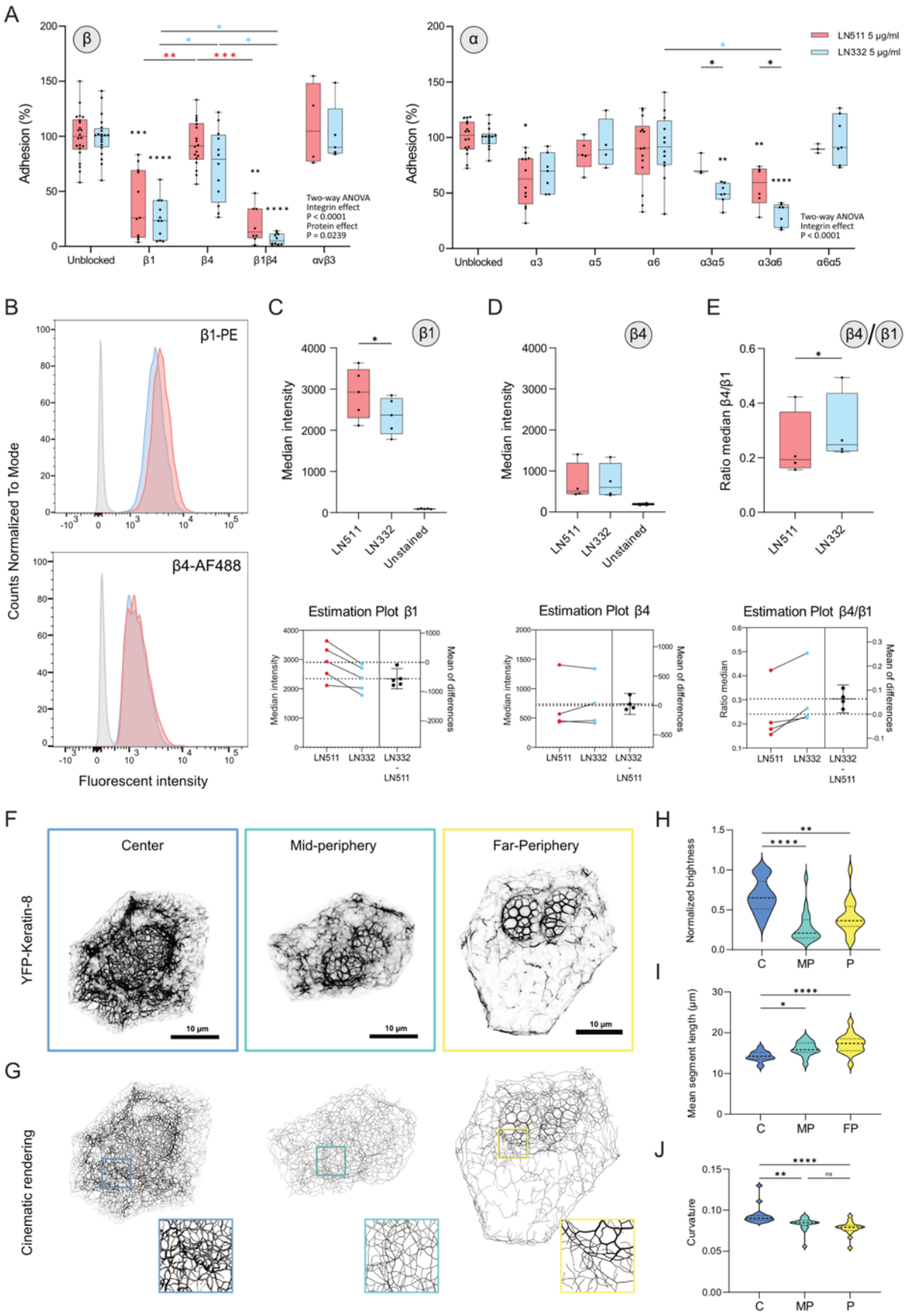
A
β
Adhesion (%)
Unblocked
β1
β4
β1β4
αvβ3
Two-way ANOVA
Integrin effect
P < 0.0001
Protein effect
P = 0.0239
α
LN511 5 μg/ml
LN332 5 μg/ml
α3
α5
α6
α3α5
α3α6
α6α5
Two-way ANOVA
Integrin effect
P < 0.0001
B
β1-PE
β4-AF488
Counts Normalized To Mode
Fluorescent intensity
C
β1
Median intensity
LN511
LN332
Unstained
Estimation Plot β1
Mean of differences
D
β4
Estimation Plot β4
E
β4/β1
Ratio median β4/β1
Estimation Plot β4/β1
Ratio median
F
Center
Mid-periphery
Far-Periphery
YFP-Keratin-8
10 μm
G
Cinematic rendering
H
Normalized brightness
C
MP
P
I
Mean segment length (μm)
FP
J
Curvature
ns

250

251

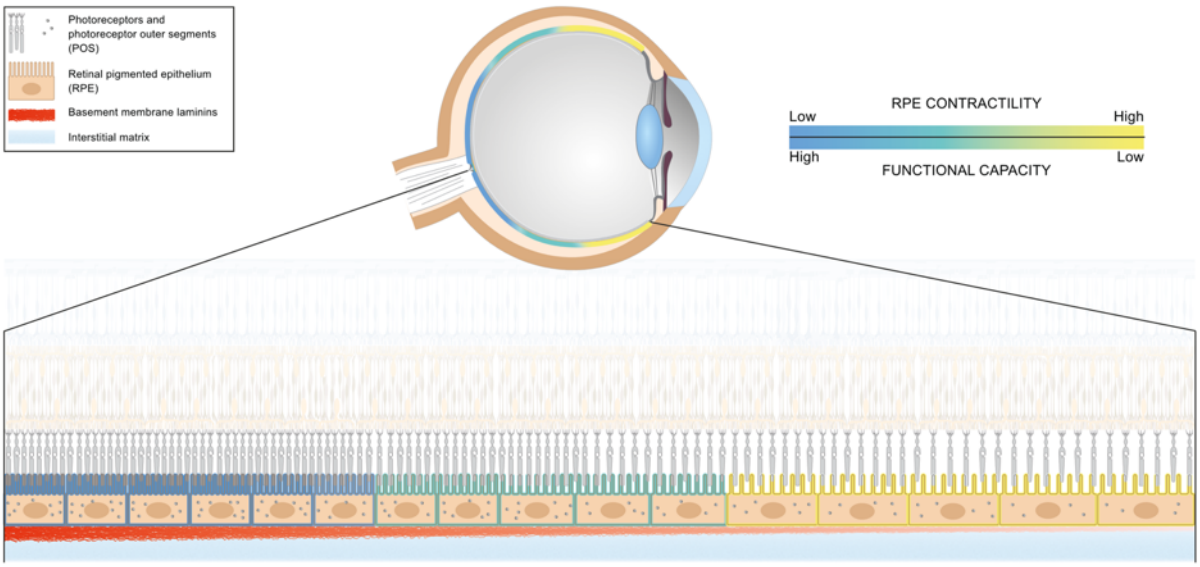

252

Figure 5: RPE mechanical homeostasis along the visual axis. *Schematics of ECM-orchestrated changes in the retinal tissue shows how high basement membrane laminin density in the macula ensures a mechanical status that supports maintaining high functional demand. Low laminin density in the retinal periphery increases RPE contractility, which correspond to diminished functional capacity.*

253

254

255 DISCUSSION

256 Our findings demonstrate a direct role of laminin density in regulating RPE functional capacity through
257 epithelial contractility. For the first time, we report the presence of a relative density gradient of specific
258 laminin isoforms in the Bruch's membrane *in vivo*. The Bruch's membrane has the highest laminin
259 content at the retinal centre, whereas at the far periphery, the laminin 332 and α5-containing isoforms
260 have the lowest density. This laminin density gradient correlates with a different topology and with a
261 gradual increase in RPE cellular shape factor with the lower laminin density corresponding to more
262 elongated cells. Cellular shape factor and cell-to-neighbourhood relationship directly correspond to
263 mechanical properties of the epithelial monolayers [18–20] and contractility [21,37,38]. Finally, the different
264 arrangements of the keratin network within the RPE imply that, towards the periphery, the actin
265 cytoskeleton has a more prominent contribution to the epithelial mechanical status. Altogether, this
266 evidence strongly indicates higher epithelial contractility at the far periphery compared to the centre.
267 Due to technical limitations for the direct *in vivo* quantification of mechanical properties and
268 contractility, we employed a human-relevant *in vitro* model using laminin-functionalized PAA gels and
269 hiPSC-derived RPE cells. The stringent condition for ECM availability and remodelling, created by the
270 PAA gel, revealed a direct role of low-density laminin 511 in increasing RPE contractility (higher traction
271 forces and monolayer stress) and reducing the epithelium efficiency to phagocyte POS. Despite this
272 increase in RPE contractility, there were no observed alterations in cell shape or topology. This
273 suggests that the monolayer topology and morphology *in vivo* may be defined by the convergence of

274 several factors, such as RPE's anchorage to the ora serrata at the retinal periphery [53]. Moreover, our
275 data rule out the exclusive role of laminins in defining RPE monolayer organization or stiffness.
276 The effect of laminin α5 on cellular mechanics is not surprising. Laminin α5 containing isoforms have
277 been shown to enhance cell stiffness and support better shear stress mechanotransduction [54] and
278 intercellular tightness [55] in the endothelium. As shown for the epithelium, also RPE cells preferentially
279 adhere to this laminin by β1 integrins (i.e., α3β1 and α6β1 integrins). This is different from laminin 332,
280 which additionally supports RPE adhesion via α6β4 integrins, i.e., hemidesmosomes. The role of
281 hemidesmosomes in organizing the keratin network is crucial for the mechanical integrity of epithelial
282 tissues [56,57] and was proposed to define their textile nature [44]. More recently, data from different labs
283 demonstrated that hemidesmosomes and the keratin network reduce cellular traction force [48] and
284 protect the nucleus from mechanical strain [49]. In agreement with the tensegrity model, cellular
285 mechanics is a balance of cytoskeleton-driven forces, where a contractile actin cytoskeleton is
286 counterbalanced by intermediate filaments [58–60]. Therefore, a higher ratio of β4/β1 integrins in RPE
287 adhering to low-density laminin 332 could explain the quantified low traction forces in contrast with
288 low-density laminin 511, which promotes higher epithelial traction. Similarly, a thinner and tenser
289 keratin network in RPE in the far periphery and elongated nuclei suggest a higher contribution of the
290 contractile actin cytoskeleton to tissue mechanics in this area. Nevertheless, technical challenges leave
291 the open question whether the relative amount of laminin isoforms differ along the visual axis and if
292 the ratio between β4 integrins (hemidesmosomes) and β1 integrins decreases with the distance from
293 the optic nerve.
294 The fact that ECM density reduction increases epithelial traction has been previously proposed based
295 on the reduction of integrin β1 receptor engagement *in vitro* [36,61]. Here, for the first time, we show the
296 physiological relevance of this density and the importance of the β4/ β1 ratio for epithelial mechanics.
297 Future studies will need to focus on dissecting the relationship between laminin receptors' density and
298 their role in regulating epithelial mechanical homeostasis. This is particularly relevant for retinal ageing,
299 given the reported reduction in hemidesmosomal attachment sites in RPE [62].
300 A study on stem cell derived RPE has previously shown that the organisation of the actin cytoskeleton
301 can predict the ability of differentiated cells to phagocyte POS [33]. Particularly, the presence of F-actin
302 stress fibres impaired the phagocytic activity of these cells. These data and our findings strongly
303 suggest that high contractility in RPE is detrimental to its homeostasis and function. RPE apical
304 microvilli interact with POS mostly via the Mer tyrosine kinase receptor (MerTK) and the integrin αvβ5
305 [63]. The activation of MerTK is thought to be involved in the inside-out activation of integrin αvβ5 with
306 the recruitment of talin, vinculin and interaction with F-actin [63]. These focal adhesion-like structures
307 have already been shown to mediate phagocytosis in macrophages and to be mechanosensitive [64].

308 Hence, the formation of this apical molecular clutch may be sensitive to the overall cellular contractility
309 defined by the ECM substrate and explains the lower efficiency of POS internalisation observed in this
310 work. Furthermore, the homophilic interaction between POS and RPE via the neural cell adhesion
311 molecule (N-CAM) may also be impacted by increased RPE contractility affecting the bond lifetime,
312 thus, binding efficiency.
313 Overall, our work underlines the important role of RPE mechanobiology for outer retina physiology
314 and opens important questions about its role in retinal ageing. ECM remodelling while ageing may
315 affect cell adhesion and shift RPE mechanical homeostasis out of its optimal range, making it more
316 prone to phenotypical changes. Overcoming this threshold may cause sight-impairing diseases such
317 as (high) myopia and age-related macular degeneration. Moreover, the use of Rho kinase inhibitors,
318 as in glaucoma treatment [65,66], may be implemented to prevent the progression of RPE-specific
319 diseases. Undoubtedly, further studies will be necessary to elucidate to what extent RPE contractility
320 is involved in outer retina diseases.
321
322 CONTRIBUTIONS
323 J.D.R. conceived the project. A.N.K. and T.P. designed and performed all the experiments. I.D. and
324 F.S. helped in establishing hiPSC-derived RPE cell culture on PAA gels. F.S. supported the integrin
325 studies. T.Pr. supported image segmentations and analyses. T.H. performed and analysed AFM
326 experiments on decellularised Bruch's membrane. M.H. and A.S. contributed to morphometric
327 analyses and interpretation of RPE monolayers *in vivo* and *in vitro*. R.W. performed the segmentation
328 and analyses of the keratin network. R.L. provided keratin 8 - YFP mice and expertise on the keratin
329 network. J.D.R. and A.N.K. wrote the manuscript, and all authors discussed and commented on it.
330
331 ACKNOWLEDGMENT
332 This work was supported by a grant from the Interdisciplinary Centre for Clinical Research within the
333 Faculty of Medicine at the RWTH Aachen University and from the German Research Foundation - DFG
334 - (grant n° RU 337 2366/3-1). Furthermore, the authors acknowledge the support of the
335 Mechanobiology in Epithelial 3D Tissue Constructs (ME3T) graduate school (GRK 2415/363055819)
336 and the DWI – Leibniz-Institute for Interactive Materials. A.N.K is supported by the Add-on Fellowship
337 of the Joachim Herz Foundation. We acknowledge the help of the Flow Cytometry Facility, a core
338 facility of the Interdisciplinary Center for Clinical Research (IZKF) Aachen within the Faculty of Medicine
339 at RWTH Aachen University. We appreciate the technical support of Adam Breitscheidel in the graphic
340 design and Gloria's excellent help in imaging.
341

342 METHODS

343 **Retina flat mount preparation.** Retina flat mounts were prepared from BALB/c mice of 25-30 weeks
344 of age. After sacrifice, the eyes were enucleated and fixed with 2% (wt/vol) paraformaldehyde (PFA)
345 for 4 hours at 4°C rotating. To best visualize the RPE layer, the eyes were prepared as flat mounts
346 according to published protocol[67]. Briefly, the cornea, the iris and the lens were removed, and the
347 eyecup was cut into eight longitudinal slices to allow its spreading. Afterwards, the neurosensory retina
348 was gently detached exposing the RPE layer adhering to its ECM for fluorescent staining and imaging.
349 The animal care and sacrifice were conducted according to the German Animal Welfare Act (LANUV,
350 reference number 84- 02.04.2015.A190).

351

352 **Atomic force microscopy of Bruch's membrane.** Upon enucleation, murine eyes were freshly
353 dissected using cold phosphate-buffered saline without Ca^{2+} and Mg^{2+} ($PBS^{-/-}$) and containing protease
354 inhibitors as instructed by the manufacturer (Roche, 4693132001). Dissected eyes were denuded by
355 the RPE layer via incubation of the tissue for 60 minutes with 50 mM Tris–HCl buffer plus 20 mM
356 ethylenediamine tetraacetic acid (EDTA), pH 7.4, followed by 20 minutes incubation in 50 mM Tris–
357 HCl buffer and two washes of 10 minutes with 1 M NaCl, pH 7.4. Each solution contained freshly added
358 cOmplete™, EDTA-free Protease Inhibitor Cocktail (Roche, 4693132001). Next, the prepared eyes
359 were glued to a surface using Corning Cell-Tak Cell and Tissue Adhesive (Corning, 354240).
360 Cantilevers with a spherical colloidal tip of 6.62 µm diameter (Nano and More GmbH, CP-PNPS-SiO-
361 C-5) were used to indent 200 nm into the decellularised Bruch's membrane in different regions of the
362 eye. The experiments were performed in a Dimension Icon atomic force microscope (Bruker Co. USA).
363 Probes were calibrated using the thermal oscillation method, built into the software (Nanoscope 9.4).
364 Force distance curves were recorded with an approach and retraction speed of 1 µm/s, with a relative
365 maximal force set typically to 2 nN. The maximal range of the Z distance was set to 2.5 µm. All curves
366 were exported to ASCII files with the analysis software of the instrument. The approach part of the
367 curves was analysed using a custom-written script in Python (https://www.python.org) using the Hertz
368 model (equation (1)). The Poisson ratio was assumed to be v = 0.3. The last 40-50% of the data points
369 are fit to a line and subtracted as background.

370

371 $$F(\delta) = \frac{4}{3}\frac{E}{1-\nu^2}\sqrt{R}(\delta - \delta_0)^{3/2} \qquad (1)$$

372

373 The model fits the whole curve using a nonlinear fit (leastsq) from Scipy (https://www.scipy.org) finding
374 both Young's modulus and the contact point. (code is available under:
375 https://github.com/tomio13/AFMforce).

376

377 **Immunofluorescence of retinal tissue.** Fluorescent staining of retina flat mounts was performed as
378 follows. After fixation and dissection, the tissue was incubated for one hour in 1% bovine serum
379 albumin (BSA) (wt/vol) in $PBS^{-/-}$ containing 0.1% (vol/vol) Triton X-100, followed by overnight staining
380 at 4°C with primary antibodies or phalloidin dissolved in $PBS^{-/-}$ solution of 1% (wt/vol) BSA and 0.1%
381 (vol/vol) Triton X-100. Secondary antibodies were diluted in $PBS^{-/-}$-containing 0.1% (vol/vol) Triton X-
382 100 and incubated with the tissue at room temperature for two hours. Finally, the retinas were
383 incubated for 15 minutes with 5 µg/ml Hoechst 33342 (Thermo-Fischer Scientific, 62249) in $PBS^{-/-}$
384 before being mounted on glass slides with Mowiol mounting medium (Sigma-Aldrich). Primary and
385 secondary antibodies used in this work are listed in supplementary table 1.

386

387 **Retinal extracellular matrix quantification.** To quantify the relative amount of ECM protein in the
388 Bruch's membrane upon immunofluorescence staining, Z-stacks (0.5 µm optical slices) from the
389 different regions were obtained using a Zeiss LSM 710 (Carl Zeiss) confocal microscope with a Plan-
390 Apochromat 63 x/1.4-NA, DIC M27 oil immersion objective using unified illumination settings. The
391 distance from the optic nerve was monitored using the automated stage of the microscope and setting
392 the optic nerve as an origin. Within the eye, Z-stacks for each region were recorded per eight
393 longitudinal slices, respectively. Mean fluorescent intensity in single optical sections identified as BrM
394 was measured using Fiji software (National Institutes of Health, USA). Manually defined regions of
395 interest (ROIs) were selected to avoid artefacts due to tissue tearing during preparation (Fig. 1 I
396 "stars"). Three to five ROIs were measured for each stack, and the fluorescence intensity of all data
397 was normalized to the highest measured value in the eye.

398

399 **Keratin-8 network segmentation and characterization.** Retinas for keratin-8 analysis were prepared
400 as flat mounts from homozygous keratin 8-YFP knock-in mice [51]. In each region (centre, mid periphery
401 and far periphery), z-stacks of six cells were recorded per animal using a Plan-Apochromat 63 x/1.4-
402 NA, DIC M27 oil immersion objective in Airyscan mode at a Zeiss LSM 710 (Carl Zeiss), for a total of
403 54 analysed cells. To ensure the analysis of only individual cells, the signal within individual cells was
404 cropped from confluent monolayers using standard tools in Fiji. Cell borders were manually defined
405 for each z-slice and the cell exterior was set to a grey value of 0. The obtained images were segmented
406 and processed to obtain a keratin network model for each cell as previously described [52] Finally,
407 custom-made Matlab scripts were used to analyse the network properties including brightness,
408 segment length and curvature [52].

409

410 **hiPSC-RPE culture.** Differentiated hiPSC-RPE were purchased cryopreserved from FUJIFILM Cellular
411 Dynamics and after thawing, seeded in 24-well plates coated with 2.5 µg/ml Vitronectin XF (StemCell
412 Technologies, 07180) at a density of 1600-1800 cells/mm^2. Cells were cultured to confluence in a
413 humidified incubator at 37°C and 5% CO_2 and then, after detachment, reconstituted in
414 CELLBANKER 2® freezing media (Amsbio LLC, 11891) and kept in liquid nitrogen for future use. Cell
415 detachment for cryopreservation or experiments was achieved through 30 minutes of incubation with
416 5 mM EDTA in PBS without Ca^{+2} and Mg^{+2} ($PBS^{-/-}$) followed by TrypLE Express dissociation agent
417 (Gibco, 12605-010) for five minutes at 37°C. Prior to seeding, cells were centrifuged at 300 g for 5
418 minutes and resuspended in the media at the desired density. For the experiments, cells were thawed
419 again and cultured for up to two weeks until confluence before use. For seeding on polyacrylamide
420 hydrogels, cells were seeded at a density of 5000-6000 cells/mm^2, corresponding to the RPE density
421 in the human macula [15] and cultured for one week. Cells were cultured in hiPSC-RPE medium
422 composed of MEM α (Thermo Fisher, 12549-089), 5% (vol/vol) knock-out serum replacement (Gibco,
423 10828-028), 1% (vol/vol) N-2 supplement (Gibco, 17502-048), 55 nM hydrocortisone (Sigma-Aldrich,
424 H6909), 250 µg/ml taurine (Sigma, T0625), 14 pg/ml triiodo-L-thyronine (Sigma, T5516) and 25 µg/ml
425 gentamicin (Gibco, 15750-060). The medium was exchanged every second day.
426
427 **Hydrogel preparation and functionalisation.** To obtain flat hydrogel substrates, a mixture of 40%
428 acrylamide (Bio-Rad, 1610140) and 2% bis-acrylamide (Bio-Rad, 1610142) in distilled water was first
429 prepared. The following ratios of acrylamide / bis-acrylamide in the mixture were used to reach
430 different hydrogel Young's moduli quantified by nanoindentation: 5 % / 0.1 % (wt/vol) for 4 kPa and
431 10% / 0.07 % (wt /vol) for 18 kPa. Then, the mixture was combined with 0.5 % of (vol/vol) ammonium
432 persulfate (Sigma Aldrich, 248614, 10 % (wt/vol) stock solution in distilled water) and 0.05 % (vol/vol)
433 N`-tetramethylethylenediamine (TEMED) (Sigma Aldrich, 411019), and pipetted between
434 glutaraldehyde-activated glass bottom petri dishes (Cellvis, D35-20-0-N) and a hydrophobic glass
435 coverslip. If hydrogels were used for traction force microscopy, 1 µm yellow-green carboxylate-
436 modified polystyrene microbeads (Sigma, L4655) were included in the solution.
437 ECM proteins were crosslinked on the hydrogels' surface according to the protocol described by
438 Przybyla L. and colleagues [34]. Briefly, for functionalisation solution, we prepared stocks of 0.5 M HEPES
439 NaOH pH6 and 0.2% (wt/vol) bis-acrylamide in distilled water, 0.2 % (vol/vol) tetramethacrylate (Sigma,
440 408360) and 3% (wt/vol) hydroxy-4'-(2-hydroxyethoxy)-2-methylpropiophenone (Sigma, 410896) in
441 ethanol. Acrylic acid N-hydroxysuccinimide ester (Sigma, A8060) was initially dissolved in DMSO (10
442 mg/ml) and later reconstituted in 50% ethanol for the final concentration of 0.03 % (wt/vol). Calculating
443 0.5 ml solution per gel, we combined 216.65 µl of sterile water, 50 µl of 0.5 M HEPES NaOH pH 6,

444 32.5 µl of ethanol and 25 µl of bis-acrylamide and degassed under vacuum for 20 min. Then, 5 µl
445 tetramethacrylate, 4.165 µl hydroxy-4′-(2-hydroxyethoxy)-2-methylpropiophenone and 5 µl of the ester
446 reconstituted in 161.65 µl of 50% ethanol were added to the degassed solution. The completed
447 functionalization solution was applied over the surface of hydrogels, previously partly dehydrated in a
448 70% ethanol solution for 5 minutes, and the hydrogels were exposed for 10 minutes to ultraviolet light.
449 After sequential double washing with 25 mM HEPES buffer and $PBS^{-/-}$ for a total of 20 minutes, the gel
450 surface was incubated overnight at 4°C with the desired ECM protein solution. Human recombinant
451 laminin-511 (Biolamina, LN511-0202) and laminin-332 (Biolamina, LN332-0202) were prepared at the
452 desired concentration in PBS containing Ca^{2+} and Mg^{2+} ($PBS^{+/+}$) mixed with 30 µg/ml collagen type IV
453 (Sigma-Aldrich, M7027-100G). Vitronectin (StemCell Technologies, 07180) was used without dilution
454 at 250 µg/ml. Finally, the obtained hydrogels were washed in $PBS^{+/+}$ and sterilized by 30 min ultraviolet
455 light irradiation before their application as cell culture substrates.
456 To represent surface protein saturation, gels were chemically crosslinked and coated with laminin-511
457 at concentrations of 5, 10, 20 or 30 µg/ml along with collagen type IV (30 µg/ml) in $PBS^{+/+}$. After
458 overnight incubation at 4°C, gels were thoroughly washed with $PBS^{+/+}$ to remove unbound protein,
459 fixed with 2% PFA for 10 minutes at room temperature, blocked with 1% BSA and stained with primary
460 Anti-mouse laminin α5 (gift from Lydia Sorokin) and secondary Anti-mouse IgG AF594 (Invitrogen,
461 A11005). Between all steps, gels were washed with $PBS^{-/-}$ for at least 1 h. Stained gels were imaged
462 with a 63x objective on ApoTome.2 Fluorescence Microscope (Carl Zeiss), with at least 10 regions per
463 gel. The average intensity of each image was measured using Fiji software, and the final results were
464 plotted in GraphPad Prism 10.
465
466 **Immunofluorescence staining of hiPSC-RPE.** Cells on hydrogels were first quickly washed with warm
467 (~37 °C) $PBS^{+/+}$ then fixed with warm (~37 °C) 2% (wt/vol) PFA for 8 minutes at room temperature.
468 After fixation, cells were permeabilized with 0.3% (vol/vol) Triton X-100 for 2 minutes and blocked with
469 1% (wt/vol) BSA for 30 minutes at room temperature. Primary antibodies or Phalloidin-iFluor 647
470 Reagent (Abcam, ab176759) in PBS containing 1% (wt/vol) BSA were incubated overnight at 4°C. The
471 following day, secondary antibodies were diluted in a PBS solution containing DAPI (1 µg/ml,
472 Invitrogen D1306) and incubated with the sample for 30 minutes at room temperature. Primary and
473 secondary antibodies used in this work are listed in supplementary table 1. The samples were imaged
474 in PBS solution to match the immersion type of the objective. Cells were imaged using Plan-
475 Apochromat 40x water immersion objective on Zeiss LSM 710 confocal microscope with Airyscan
476 capability (Carl Zeiss).
477

478 **Live staining.** For live imaging of F-actin, hiPSC-RPE cells cultured on PAA gels were incubated with
479 500 nM of a fluorogenic F-actin probe SirActin (Spirochrome, SC001) containing medium for at least
480 two hours before imaging. The samples were imaged using Plan-Apochromat 40x water immersion
481 objective on Zeiss LSM 710 confocal microscope with Airyscan capability (Carl Zeiss). Orthogonal views
482 from Z-stacks acquired via confocal live-imaging of F-actin (SirActin) were used to measure the average
483 junctional height of cultured RPE monolayers using Fiji image processing package (National Institutes
484 of Health, USA).
485
486 **Morphometric and topology analyses.** Microscopy images of RPE *in vivo* and *in vitro* were segmented
487 using the cellpose software [68] (www.cellpose.org) applied on F-Actin micrographs. Segmented cells
488 were imported into Fiji as ROIs and used to generate skeletonised images. The skeletonised images
489 were then imported into custom-written MATLAB software [69]. Prior to analysis, the software removes
490 15 pixels on the sides of the images to remove poor mask definition by cellpose (Sup. fig. 1 B), and
491 then applies a Gaussian filter with a standard deviation of 2 pixels (function "imgaussfilt") to correct
492 the pixel connectivity on the masks provided by cellpose. Finally, the software extracts information
493 about the cell morphology (cell area, perimeter, and elongation) and topology (cell neighbours) as
494 previously described [69]. For these analyses, the cells at the edge of the picture were not considered to
495 avoid any segmentation error (Sup. fig. 1 C). For *in vivo* images, in total, 24 images from 3 different
496 mice have been analysed for the "centre" and "mid periphery" regions of the retina (8 images each)
497 and 23 images for the "far periphery" region (8-8-7 images for the 3 mice respectively). This
498 corresponds to a total cell number of 5575 cells for the centre, 7957 for the mid periphery and 7863
499 for the far periphery. For *in vitro* images, 71 images were analysed (at least 2 images per experiment).
500 Each image provided in between 86 and 312 cells. Because of segmentation error, to remove
501 unnaturally large cells, cells with a rescaled area (see below) higher than 2, and cells with a
502 neighbourhood larger than 10 cells have been removed from the analysis. The number of cells per
503 condition is summarised in supplementary table 2. To build both Lewis' and Desh' law, data were
504 separated with respect to their number of neighbours and binned in different classes before being
505 averaged. To build Aboav-Weaire's law, the cells at the images' edge were removed, since their
506 neighbourhood is not defined. For that, the neighbourhood of each cell is reconstructed to determine
507 the average position of the collection of neighbours. If the distance between their average position
508 and the central cells is less than 30 px, the central cell is assumed to be in the bulk of the image and
509 not on the border of the image. To plot Aboav-Weaire's law, we computed b(n) defined in (2).
510
511 $$b(n) = (n-6)\mu_{m(n)} - \sigma_n^2 \qquad (2)$$

512 where $\mu_{m(n)}$ is the mean size of the neighbourhood among the neighbours, and σ_n^2 is the central second
513 moment of the distribution of neighbours, i.e., its variance. Such distribution is taken for a given mouse,
514 not among different mice. Data from the different mice are average together with a ponderation
515 proportional to the total number of cells making the statistics.
516
517 **Scanning Electron Microscopy** (Critical Point Drying). After a week in culture on a polyacrylamide gel
518 with the defined coating, hiPSC-RPE were fixed in 3% glutaraldehyde (Agar scientific, Wetzlar,
519 Germany) for 4 h at 4°C followed by a washing in 0.1 M Soerensen's Phosphate Buffer (Merck,
520 Darmstadt, Germany). The dehydrating step was performed in the ascending alcohol series with 10
521 minutes duration each. The samples were sequentially immersed in the following solutions: 30%
522 ethanol, 50% ethanol, 70% ethanol, 90% ethanol, and three times in 100% ethanol. Critical Point
523 Drying was performed in liquid CO2. Prior to imaging, cell monolayers were coated with 10 nm
524 gold/palladium layer.
525
526 **Proliferation assay.** Levels of proliferation in hiPSC-RPE monolayers were assessed using a
527 proliferation assay kit Click-iT EdU (Thermo Fisher, C10337). Cells were incubated with a 1:1 mixture
528 of cell culture supernatant and 5-Ethinyl-2'-Desoxyuridin (EdU) (20 µM) containing hiPSC-RPE cell
529 culture medium for 24 h. Final EdU concentration in the mixture was 10 µM. Afterwards, cells were
530 fixed as described for immunofluorescent labelling and processed according to the manufacturer's
531 instructions. As EdU incorporates into newly synthesized DNA, proliferating cells were identified as
532 having their nucleus positively stained with EdU-Alexa Fluor 488. The total area of the gel was imaged
533 on Axio Observer 7 (Carl Zeiss) microscope as an overview using the tiles option. The ratio of
534 proliferating cells was calculated in comparison with DAPI-positive nuclei and quantified using the
535 particle analysis plugin of Fiji software (National Institutes of Health, USA).
536
537 **Photoreceptor outer segment internalisation assay**. Photoreceptor outer segments (POS) were
538 isolated in batches from porcine eyes from a local slaughterhouse as previously described [70]. Briefly,
539 the eyes were dissected using a red safelight lamp as the only illumination source, and the neural retina
540 was collected. After retinal mechanical homogenisation, POS were isolated via ultracentrifugation in a
541 sucrose gradient. Thereafter, POS were labelled with 2.5 mg/ml FITC dye (Thermo Fisher, F1906),
542 resuspended in DMEM (Thermo Fisher, 31331-028) containing 2.5% sucrose and stored in aliquots at
543 -80 °C for future use. For internalisation assay, POS aliquots were thawed in a water bath, washed with
544 medium, centrifuged at 2300g for 5 min and resuspended in hiPSC-RPE cell medium to an amount of
545 roughly 10 POS per RPE cell in culture. Human MGF-E8 protein (R&D Systems, 2767-MF-050) and

546 human protein-S (Coachrom, pp012A) were added at respectively 2.4 µg/ml and 2 µg/ml to aid the
547 internalisation. Next, hiPSC-RPE monolayers were washed twice with warm media and incubated for
548 four hours at 37°C with the prepared mixture at a density of approximately ten POS per cell. After
549 incubation, the monolayers were gently washed four times with warm $PBS^{+/+}$ and fixed for fluorescence
550 staining as described. Phagocytosis efficiency was calculated as projected area of internalised POS
551 divided by the total projected POS area in the same field of view. Internalised POS were identified in
552 orthogonal views from confocal optical sections (0.5 µm) by using F-actin staining to distinguish
553 between apical-bound and internalised segments. Analyses were automatised with the particle
554 analyses plugin of Fiji software (National Institutes of Health, USA) after applying a binary mask on the
555 images.
556
557 **Traction force and monolayer stress microscopy.** Traction force quantification and monolayer stress
558 calculations were performed as previously described [36,37]. Briefly, a week-old monolayer cultured on a
559 PAA gel substrate containing fluorescent beads was imaged using Axio Observer 7 (Carl Zeiss)
560 microscope for the beads signal. Then, the monolayer was detached with 0.5% SDS solution in $PBS^{-/-}$
561 followed by washing steps and 20 minutes of gel incubation in cell media to prevent gel shrinkage due
562 to the solvent change. The positions of the fluorescent beads in the hydrogel after the cell detachment
563 (relaxed state of the gel) were compared with the tense gel before, and beads displacement vectors
564 were calculated using the particle image velocimetry (PIV) plugin of Fiji (National Institutes of Health,
565 USA). Traction forces were calculated from these vectors using the Fourier transform traction cytometry
566 plugin (FTTC) of Fiji (National Institutes of Health, USA). Next, based on the traction force information,
567 average normal stress vectors were calculated using a force balance algorithm in MATLAB (MathWorks)
568 as formulated elsewhere [36,37]. For each measured sample, the average cell height was calculated using
569 a live actin staining (SirActin, Spirochrome) to correctly input the force balance algorithm.
570
571 **Stiffness measurements of hiPSC-RPE monolayers.** Measurements were performed using a Chiaro
572 Nanoindenter System (Optics 11 Life) mounted on Zeiss Axio Observer 7 (Carl Zeiss) with an
573 environmental chamber sustaining 37°C. A probe of 10 µm radius and 0.025 N/m stiffness (Optics 11
574 Life) was used and the indentation was performed in Displacement control mode, indenting 10 µm
575 into the cell monolayer. Approach curves were fitted via the DataViewer V2.4.0 software (Optics 11
576 Life) using a Hertzian contact model according to a set indentation depth from 0 to 3 µm for the apical
577 stiffness. A Poisson's ratio of 0.5 was used and a maximum load of 30% was allowed for setting the
578 contact point. Only results from well fitted data ($R^2 > 0.95$) were considered for statistics.
579

580 **Drug experiments.** For activation of the RhoA-dependent pathways, we incubated RPE monolayers
581 with Rho activator II (Cytoskeleton, CN03-A) and Rho kinase (ROCK) inhibitor Y-27632 (Sigma Aldrich,
582 Y0503)[71]. Briefly, the one-week-old RPE monolayers on a hydrogel coated with high laminin density
583 (20 µg/ml) were treated with Rho activator II (1 µg/ml) containing media for 3 hours prior to POS
584 phagocytosis assay or traction force measurements to promote the actomyosin contractility, or with an
585 equal volume of water as a solvent control. To reduce the actomyosin contractility at low laminin
586 surface density (2.5 µg/ml), ROCK inhibitor (25 µM) was added to the media one hour prior the POS
587 phagocytosis assay or traction force measurements. An equal volume of DMSO was used as a solvent
588 control. Further analysis was performed as described in the relevant chapters.
589
590 **Adhesion assay.** For cell adhesion assay, a confluent monolayer of hiPSC-RPE cells cultured in a 24-
591 well plate was detached with 30 minutes incubation of 750µl of 5 mM EDTA in $PBS^{-/-}$ without enzymatic
592 treatment to prevent unwanted receptor cleavage. Cells were gently washed with an additional 750 µl
593 of EDTA in $PBS^{-/-}$ and the whole solution was transferred into the 15 ml Falcon tube. After cell counting,
594 the suspension was centrifuged at 300 g for 5 minutes. The pellet was resuspended in ice-cold media
595 in half the volume required for the experiment and transferred to low protein binding tubes. Ice-cold
596 media should contain 20 µg/ml blocking antibody for blocking experiments. After 15 minutes of
597 incubation on ice, the cell suspension was diluted (1:2) with the equivalent volume of warm media and
598 immediately transferred onto the hydrogel surface. After 15 minutes at 37°C and 5% CO_2, hydrogel
599 surfaces were gently washed with warm $PBS^{+/+}$ to remove not attached cells, fixed with 2% PFA at
600 room temperature for 8 minutes, and stained for F-Actin (Phalloidin-iFluor 488 Reagent, Abcam -
601 ab176753) for analysis. The number of attached cells was quantified using the particle analysis plugin
602 in Fiji software and normalised to the mean of control samples to convert as a percentage of adhesion.
603 The following azide-free blocking antibodies were used: integrin β1 (clone P5D2) (Santa Cruz, sc-13590
604 L), integrin β4 (clone ASC-8) (Merk, MAB2059Z), integrin αvβ3 (clone LM609) (Merk, MAB1976Z),
605 integrin α3 (clone P1B5) (Merk, MAB1952Z), integrin α5 (clone P1D6) (Merk, MAB1956Z), integrin α6
606 (clone GOH3) (Santa Cruz, sc-19622 L).
607
608 **Flow cytometry.** One-week-old hiPSC-RPE cells were carefully detached from the hydrogel substrate
609 by incubation with 10 mM EDTA in $PBS^{-/-}$ at 37°C and 5% CO_2 for 30 minutes, followed by Accutase
610 solution (Sigma Aldrich, A6964) for 15 minutes. During this period, gentle shaking was beneficial for
611 detachment. Cells were gently washed from the surface with an additional 1 ml of EDTA in $PBS^{-/-}$,
612 transferred into the 15 ml tube and centrifuged for 5 minutes at 300 g. After centrifugation, cells were
613 dispersed in ice-cold $PBS^{-/-}$ and divided into two separate tubes: one will contain the whole antibody
614 panel, and another will be stained for β4 integrin alone. For the first tube, the viability staining with

615 LIVE/DEAD™ Fixable Near IR(780) Viability Kit (Thermo Fisher Scientific, L34992) was performed
616 during the 15-minute incubation on ice protected from the light. After centrifugation at 300 g for 4
617 minutes, cells were fixed with 1 ml of 1% PFA for 5 minutes on ice and resuspended in 100 µl of $PBS^{-/-}$
618 containing 3% BSA and 5 mM EDTA (FACS buffer) for 6 minutes centrifugation at 300 g. Fluorescently
619 conjugated antibodies (see table 1) were added according to the manufacturer's instructions and
620 incubated with cells for 45 minutes on ice protected from the light. After washing, cells were
621 resuspended in 400 µl of the FACS buffer and filtered using the Flowmi(R) Cell Strainer (MERK,
622 BAH136800040) directly into the flow cytometry tube for the measurements. Stained cells were
623 analysed using a BD LSRFortessa flow cytometer equipped with 405, 488, 561 and 640 nm lasers.
624 Analysis of the data was carried out using the FlowJo software.
625
626 **Statistics.** Statistical analysis was performed using Prism (GraphPad). Data were tested for normality
627 before proceeding to further statistical analyses. Sample conditions and the specific test used for
628 each data set are indicated in corresponding figure captions.

629 REFERENCES

630

631 1. Anlaş, A. A. & Nelson, C. M. Tissue mechanics regulates form, function, and dysfunction. *Curr Opin*
632 *Cell Biol* **54**, 98–105 (2018).
633 2. Ayad, N. M. E., Kaushik, S. & Weaver, V. M. Tissue mechanics, an important regulator of
634 development and disease. Philosophical Transactions Royal Soc B 374, 20180215 (2019).
635 3. Eichinger, J. F. et al. Mechanical homeostasis in tissue equivalents: a review. Biomech Model
636 Mechan 20, 833–850 (2021).
637 4. Humphrey, J. D., Dufresne, E. R. & Schwartz, M. A. Mechanotransduction and extracellular matrix
638 homeostasis. Nat Rev Mol Cell Biology 15, 802–12 (2014).
639 5. Kozyrina, A. N., Piskova, T. & Di Russo, J. Mechanobiology of Epithelia From the Perspective of
640 Extracellular Matrix Heterogeneity. Frontiers Bioeng Biotechnology 8, 596599 (2020).
641 6. Booij, J. C., Baas, D. C., Beisekeeva, J., Gorgels, T. G. M. F. & Bergen, A. A. B. The dynamic nature
642 of Bruch's membrane. Prog Retin Eye Res 29, 1–18 (2010).
643 7. Raymond, S. M. & Jackson, I. J. The retinal pigmented epithelium is required for development and
644 maintenance of the mouse neural retina. Curr Biol 5, 1286–1295 (1995).
645 8. German, O., Buzzi, E., Rotstein, N., Rodriguez-Boulan, E. & Politi, L. Retinal pigment epithelial cells
646 promote spatial reorganization and differentiation of retina photoreceptors. J Neurosci Res 86,
647 3503–3514 (2008).
648 9. Bok, D. The retinal pigment epithelium: a versatile partner in vision. J Cell Sci 1993, 189–195 (1993).
649 10. Strauss, O. The Retinal Pigment Epithelium in Visual Function. Physiol Rev 85, 845–881 (2005).
650 11. Lakkaraju, A. et al. The Cell Biology of the Retinal Pigment Epithelium. Prog Retin Eye Res 78,
651 100846 (2020).
652 12. Young, R. W. & Bok, D. Partecipation of the Retinal Pigment Epithelium in the Rod Outer Segment
653 Renewal Process. J Cell Biology 42, 392–403 (1969).
654 13. Wald, G. & Brown, P. K. Synthesis and Bleaching of Rhodopsin. Nature 177, 174–176 (1956).
655 14. Volland, S., Esteve-Rudd, J., Hoo, J., Yee, C. & Williams, D. S. A Comparison of Some
656 Organizational Characteristics of the Mouse Central Retina and the Human Macula. Plos One 10,
657 e0125631 (2015).
658 15. Bhatia, S. K. et al. Analysis of RPE morphometry in human eyes. Mol Vis 22, 898–916 (2016).
659 16. Kim, Y.-K. et al. Morphometric Analysis of Retinal Pigment Epithelial Cells From C57BL/6J Mice
660 During Aging. Invest Ophth Vis Sci 62, 32 (2021).
661 17. Ortolan, D. et al. Single-cell–resolution map of human retinal pigment epithelium helps discover
662 subpopulations with differential disease sensitivity. Proc. Natl. Acad. Sci. 119, e2117553119 (2022).

663 18. Hannezo, E., Prost, J. & Joanny, J.-F. Theory of epithelial sheet morphology in three dimensions.
664 Proc National Acad Sci 111, 27–32 (2014).
665 19. Alt, S., Ganguly, P. & Salbreux, G. Vertex models: from cell mechanics to tissue morphogenesis.
666 Philosophical Transactions Royal Soc B Biological Sci 372, 20150520 (2017).
667 20. Kaliman, S. et al. Mechanical Regulation of Epithelial Tissue Homeostasis. Phys Rev X 11, 031029
668 (2021).
669 21. Bi, D., Lopez, J. H., Schwarz, J. M. & Manning, M. L. A density-independent rigidity transition in
670 biological tissues. Nat Phys 11, 1074–1079 (2015).
671 22. Lewis, F. T. A comparison between the mosaic of polygons in a film of artificial emulsion and the
672 pattern of simple epithelium in surface view (cucumber epidermis and human amnion). Anat Rec
673 50, 235–265 (1931).
674 23. Lewis, F. T. The correlation between cell division and the shapes and sizes of prismatic cells in the
675 epidermis of cucumis. Anat Rec 38, 341–376 (1928).
676 24. Chiu, S. N. Aboav-Weaire's and Lewis' laws—A review. Mater Charact 34, 149–165 (1995).
677 25. Kim, S., Cai, M. & Hilgenfeldt, S. Lewis' law revisited: the role of anisotropy in size–topology
678 correlations. New J Phys 16, 015024 (2014).
679 26. Rivier, N. Statistical crystallography Structure of random cellular networks. Philosophical Mag Part
680 B 52, 795–819 (2006).
681 27. Aboav, D. A. The arrangement of cells in a net. Metallography 13, 43–58 (1980).
682 28. Aboav, D. A. The arrangement of grains in a polycrystal. Metallography 3, 383–390 (1970).
683 29. Weaire, D. Some remarks on the arrangement of grains in a polycrystal. Metallography 7, 157–160
684 (1974).
685 30. Chong, N. H. V. et al. Decreased Thickness and Integrity of the Macular Elastic Layer of Bruch's
686 Membrane Correspond to the Distribution of Lesions Associated with Age-Related Macular
687 Degeneration. Am J Pathology 166, 241–251 (2005).
688 31. Newsome, D. A., Huh, W. & Green, W. R. Bruch's membrane age-related changes vary by region.
689 Curr Eye Res 6, 1211–1221 (1987).
690 32. Song, M. J. et al. Bioprinted 3D outer retina barrier uncovers RPE-dependent choroidal phenotype
691 in advanced macular degeneration. Nat Methods 20, 149–161 (2023).
692 33. Müller, C., Charniga, C., Temple, S. & Finnemann, S. C. Quantified F-Actin Morphology Is
693 Predictive of Phagocytic Capacity of Stem Cell-Derived Retinal Pigment Epithelium. Stem Cell Rep
694 10, 1075–1087 (2018).
695 34. Przybyla, L., Lakins, J. N., Sunyer, R., Trepat, X. & Weaver, V. M. Monitoring developmental force
696 distributions in reconstituted embryonic epithelia. Methods 94, 101–113 (2016).

697 35. Funaki, M. & Janmey, P. A. Biology and Engineering of Stem Cell Niches. Part Iii Des Smart
698 Biomaterials Mimic Control Stem Cell Niche 363–373 (2017) doi:10.1016/b978-0-12-802734-
699 9.00023-8.
700 36. Di Russo, J. et al. Integrin **α**5**β**1 nano-presentation regulates collective keratinocyte migration
701 independent of substrate rigidity. Elife 10, e69861 (2021).
702 37. Vishwakarma, M. et al. Mechanical interactions among followers determine the emergence of
703 leaders in migrating epithelial cell collectives. Nat Commun 9, 3469 (2018).
704 38. Park, J.-A. A. et al. Unjamming and cell shape in the asthmatic airway~epithelium. Nat Mater 14,
705 1040–8 (2015).
706 39. Malinverno, C. et al. Endocytic reawakening of motility in jammed epithelia. Nat Mater 16, 587
707 (2017).
708 40. Palamidessi, A. et al. Unjamming overcomes kinetic and proliferation arrest in terminally
709 differentiated cells and promotes collective motility of carcinoma. Nat Mater 18, 1252–1263 (2019).
710 41. Balcioglu, H. E. et al. A subtle relationship between substrate stiffness and collective migration of
711 cell clusters. Soft Matter 16, 1825–1839 (2020).
712 42. Mongera, A. et al. A fluid-to-solid jamming transition underlies vertebrate body axis elongation.
713 Nature (2018) doi:10.1038/s41586-018-0479-2.
714 43. Pérez-González, C. et al. Mechanical compartmentalization of the intestinal organoid enables crypt
715 folding and collective cell migration. Nat Cell Biol 1–13 (2021) doi:10.1038/s41556-021-00699-6.
716 44. Di Russo, D., Magin, T. M. & Leube, R. E. A keratin code defines the textile nature of epithelial
717 tissue architecture. Curr. Opin. Cell Biol. 85, 102236 (2023).
718 45. Alberts, B. et al. Molecular Biology of the Cell. 43–108 (2017) doi:10.1201/9781315735368-2.
719 46. Aumailley, M. The laminin family. Cell Adhes Migr 7, 48–55 (2012).
720 47. Hynes, R. O. Integrins Bidirectional, Allosteric Signaling Machines. Cell 110, 673–687 (2002).
721 48. Wang, W. et al. Hemidesmosomes modulate force generation via focal adhesions. J Cell Biol 219,
722 e201904137 (2020).
723 49. Kechagia, Z. et al. The laminin–keratin link shields the nucleus from mechanical deformation and
724 signalling. Nat. Mater. 1–12 (2023) doi:10.1038/s41563-023-01657-3.
725 50. Moch, M. & Leube, R. E. Hemidesmosome-Related Keratin Filament Bundling and Nucleation. Int.
726 J. Mol. Sci. 22, 2130 (2021).
727 51. Schwarz, N., Windoffer, R., Magin, T. & Leube, R. Dissection of keratin network formation, turnover
728 and reorganization in living murine embryos. Sci Rep-uk 5, 9007 (2015).
729 52. Windoffer, R. et al. Quantitative mapping of keratin networks in 3D. Elife 11, e75894 (2022).

730 53. Nobeschi, L., Freymuller, E. & Smith, R. L. Intercellular Junctions in Rabbit Eye Ora Serrata.
731 Anatomia Histologia Embryologia 35, 287–292 (2006).
732 54. Di Russo, J. et al. Endothelial basement membrane laminin 511 is essential for shear stress
733 response. Embo J 36, 183–201 (2016).
734 55. Song, J. et al. Endothelial Basement Membrane Laminin 511 Contributes to Endothelial Junctional
735 Tightness and Thereby Inhibits Leukocyte Transmigration. Cell Reports 18, 1256–1269 (2017).
736 56. Hahn, B.-S. & Labouesse, M. Tissue integrity: Hemidesmosomes and resistance to stress. Curr Biol
737 11, R858–R861 (2001).
738 57. Todorović, V., Kligys, K. R., Dusek, R. L., Jones, J. C. R. & Green, K. J. Encyclopedia of Biological
739 Chemistry (Second Edition). Cell Archit Funct Article Titles D 636–643 (2013) doi:10.1016/b978-0-
740 12-378630-2.00472-2.
741 58. Broussard, J. A. et al. Scaling up single-cell mechanics to multicellular tissues – the role of the
742 intermediate filament–desmosome network. J Cell Sci 133, jcs228031 (2020).
743 59. Ingber, D. E., Wang, N. & Stamenović, D. Tensegrity, cellular biophysics, and the mechanics of
744 living systems. Rep Prog Phys 77, 046603 (2014).
745 60. Rölleke, U., Kumari, P., Meyer, R. & Köster, S. The unique biomechanics of intermediate filaments
746 – From single filaments to cells and tissues. Curr. Opin. Cell Biol. 85, 102263 (2023).
747 61. Oria, R. et al. Force loading explains spatial sensing of ligands by cells. Nature 552, 219–224 (2017).
748 62. Anderson, R. E., Vail, M. M. L. & Hollyfield, J. G. Degenerative Diseases of the Retina. 1, (1995).
749 63. Kwon, W. & Freeman, S. A. Phagocytosis by the Retinal Pigment Epithelium: Recognition,
750 Resolution, Recycling. Front Immunol 11, 604205 (2020).
751 64. Jaumouillé, V., Cartagena-Rivera, A. X. & Waterman, C. M. Coupling of β2 integrins to actin by a
752 mechanosensitive molecular clutch drives complement receptor-mediated phagocytosis. Nat Cell
753 Biol 21, 1357–1369 (2019).
754 65. Al-Humimat, G., Marashdeh, I., Daradkeh, D. & Kooner, K. Investigational Rho Kinase Inhibitors for
755 the Treatment of Glaucoma. J. Exp. Pharmacol. 13, 197–212 (2021).
756 66. Mandell, K. J., Kudelka, M. R. & Wirostko, B. Rho kinase inhibitors for treatment of glaucoma.
757 Expert Rev. Ophthalmol. 6, 611–622 (2011).
758 67. Claybon, A. & Bishop, A. J. R. Dissection of a Mouse Eye for a Whole Mount of the Retinal Pigment
759 Epithelium. J Vis Exp (2011) doi:10.3791/2563.
760 68. Stringer, C., Wang, T., Michaelos, M. & Pachitariu, M. Cellpose: a generalist algorithm for cellular
761 segmentation. Nat Methods 18, 100–106 (2021).

762 69. Kaliman, S., Jayachandran, C., Rehfeldt, F. & Smith, A.-S. Limits of Applicability of the Voronoi
763 Tessellation Determined by Centers of Cell Nuclei to Epithelium Morphology. Front Physiol 7, 551
764 (2016).
765 70. Parinot, C., Rieu, Q., Chatagnon, J., Finnemann, S. C. & Nandrot, E. F. Large-Scale Purification of
766 Porcine or Bovine Photoreceptor Outer Segments for Phagocytosis Assays on Retinal Pigment
767 Epithelial Cells. J Vis Exp (2014) doi:10.3791/52100.
768 71. Mao, Y. & Finnemann, S. C. Acute RhoA/Rho Kinase Inhibition Is Sufficient to Restore Phagocytic
769 Capacity to Retinal Pigment Epithelium Lacking the Engulfment Receptor MerTK. Cells 10, 1927
770 (2021).
771
772

773 SUPPLEMENTARY INFORMATION

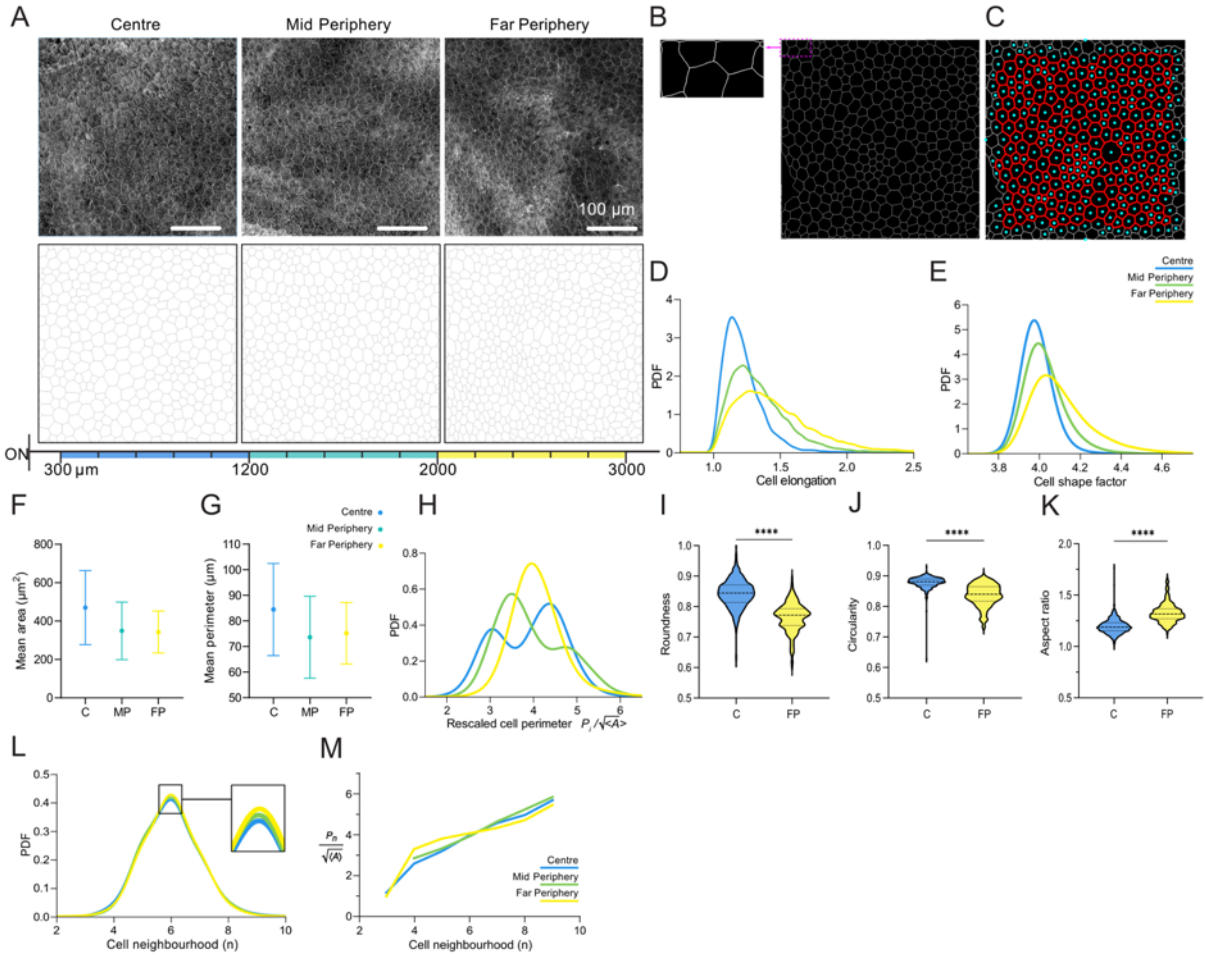

774

Supplementary figure 1: Murine RPE represents spatially different monolayer organisation. ***(A)*** *Representative confocal images of RPE stained for F-actin (top row) and post-processed binary images obtained by skeletisation used for the morphometric characterisation upon segmentation (bottom row). Scale bar 100 µm.* ***(B)*** *Representative segmentation artefacts generated with Cellpose at the image edge.* ***(C)*** *The resulting cells (blue) and neighbourhood (red) considered in the analyses. Probability density function (PDF) of cell elongation* ***(D)*** *and cell shape factor* ***(E)*** *for different retinal regions. The average cellular area* ***(F)*** *and perimeter* ***(G)*** *shown with mean value and standard deviation for each region, respectively.* ***(H)*** *PDF of the rescaled cell perimeters defined as* $P_i/\sqrt{<A>}$*, Pi being the individual cell perimeter. Nuclear geometric parameters such as roundness* ***(I)****, circularity* ***(J)*** *and elliptical aspect ratio* ***(K)*** *show significant difference for cells from centre versus far periphery. Topological characteristics of the RPE monolayer such as PDF of cell neighbourhood* ***(L)*** *and Desh's law* ***(M)*** *representing the relationship between cellular perimeter and shape varying for three different regions. All data were collected from at least 3 mice.*

775
776

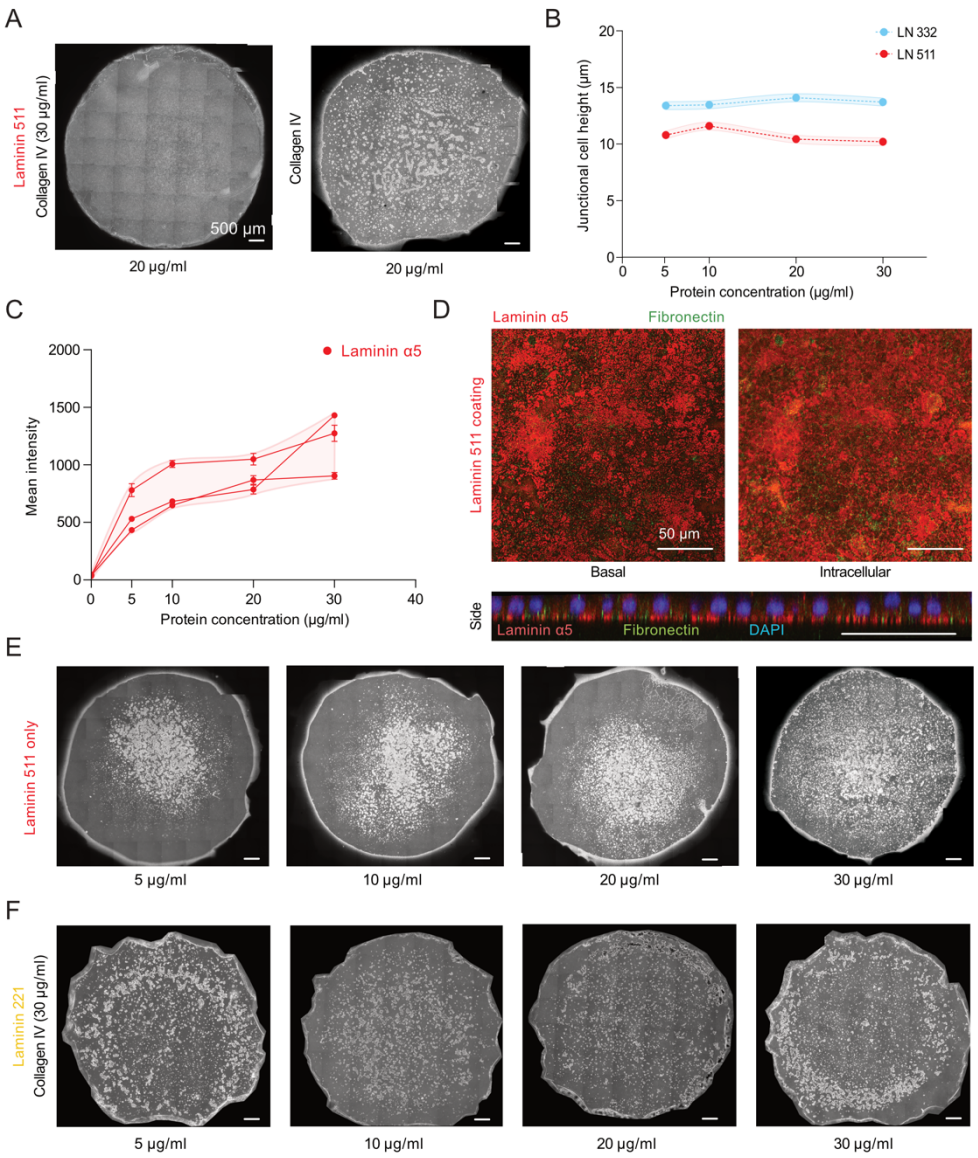

Supplementary figure 2: Protein composition of polyacrylamide gel surface coating is crucial for cell adhesion strength. ***(A)*** *Representative image of complete hiPSC-RPE monolayer obtained on 4 kPa polyacrylamide gel coated with laminin 511 (20 µg/ml) combined with collagen type IV (30 µg/ml) in contrast with the fragmented monolayer on pure collagen type IV (20 µg/ml). Scale bar 500 µm.* ***(B)*** *Average cell height measured at the adherence junction levels of one-week old hiPSC-RPE monolayer. Measurements are means from at least three independent experiments ± SEM.* ***(C)*** *Line graph of the mean fluorescent intensity of the hydrogel surface fixed and stained with laminin α5 antibody right after chemical crosslinking with different concentrations of laminin 511 combined with collagen type IV (30 µg/ml). This relation indicates correlation between laminin concentration and surface density. Each line represents individual dilution series. Images were taken from 10 different areas of the gel. Data are shown as mean ± SEM.* ***(D)*** *Immunofluorescent images of the laminin 511 coated gel surface stained for ECM proteins show the absence of fibronectin protein deposition after one week in cellular culture. Top row represents the signal from laminin α5 (red) and fibronectin (green) at the basal surface and within the monolayer. Fibronectin signal appears to be intracellular as shown in the side view of the monolayer.* ***(E, F)*** *Representative overview images of colonies hiPSC-RPE cells seeded on gels coated with different concentrations of laminin 511 and laminin 221 combined with collagen type IV (30 µg/ml), indicating the insufficient cellular adhesion and monolayer formation in contrast to standard experimental conditions. Scale bar 500 µm.*

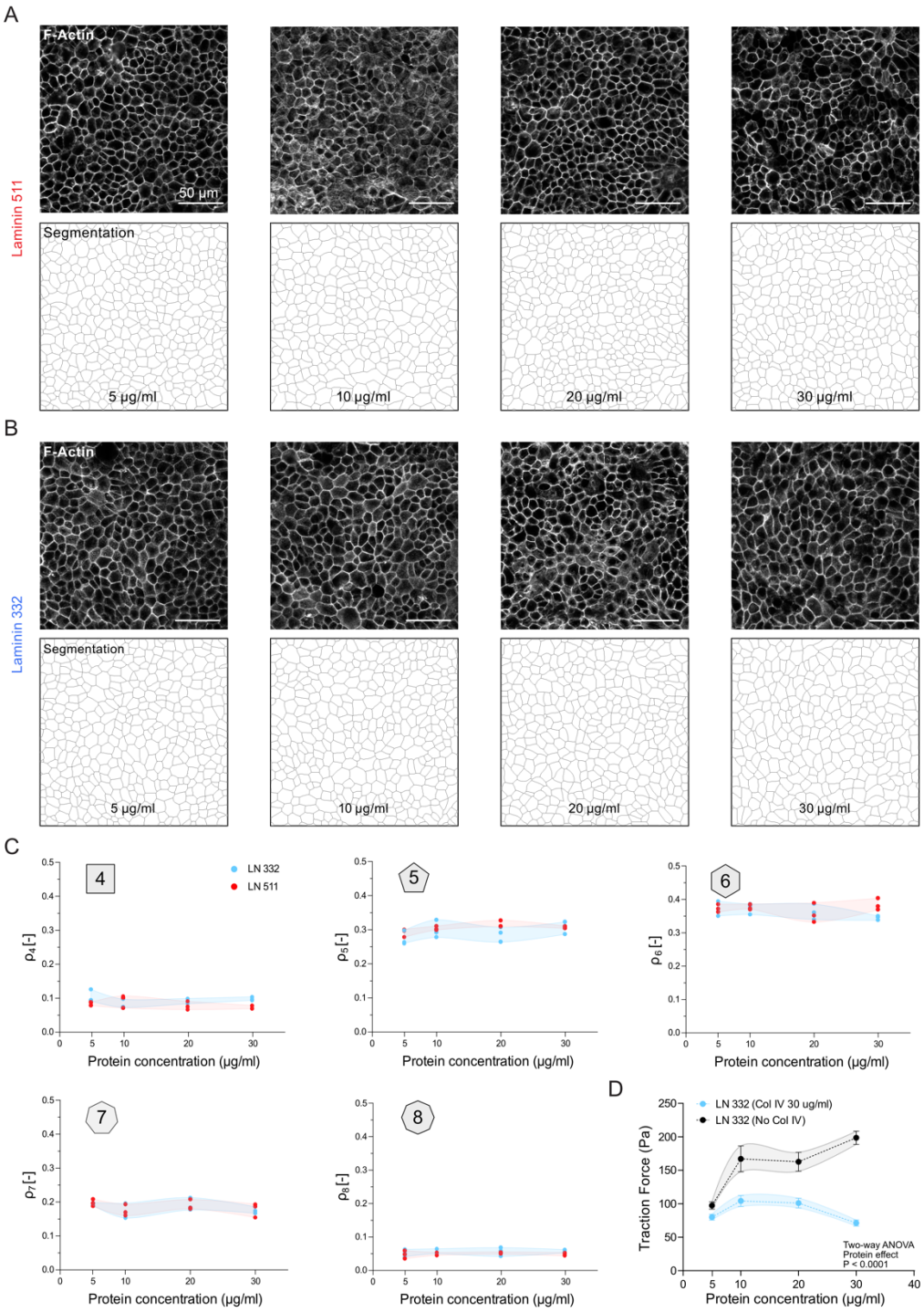

779

Supplementary figure 3: Structure and topological stability of RPE in vitro. *Representative confocal images of one-week cultured hiPSC-RPE monolayers on 4 kPa PAA gels coated with different concentrations of laminin 511* ***(A)*** *or laminin 332* ***(B)*** *both in presence of collagen type IV (30 µg/ml). The top row represents the actin cytoskeleton network in the stained samples and the bottom row shows segmented images used for morphometric analysis.* ***(C)*** *Probabilities of the cellular neighbourhood (ρ_n) from 4 (ρ_4) "squares" to 8 (ρ_8) "octagon" indicating the stable neighbourhood environment regardless of the protein surface concentration. Data are from 3 independent experiments with 3 independent fields of view in each experiment.* ***(D)*** *The presence of collagen type IV in the laminin 332 containing coating solution decreases the traction forces exerted by cells. This difference becomes less significant at lower laminin concentration. Data are shown as mean ± SEM. $P < 0.0001$ for the protein effect using mixed-effects model (REML) with the Geisser-Greenhouse correction and Tuckey's multiple comparisons test.*

780

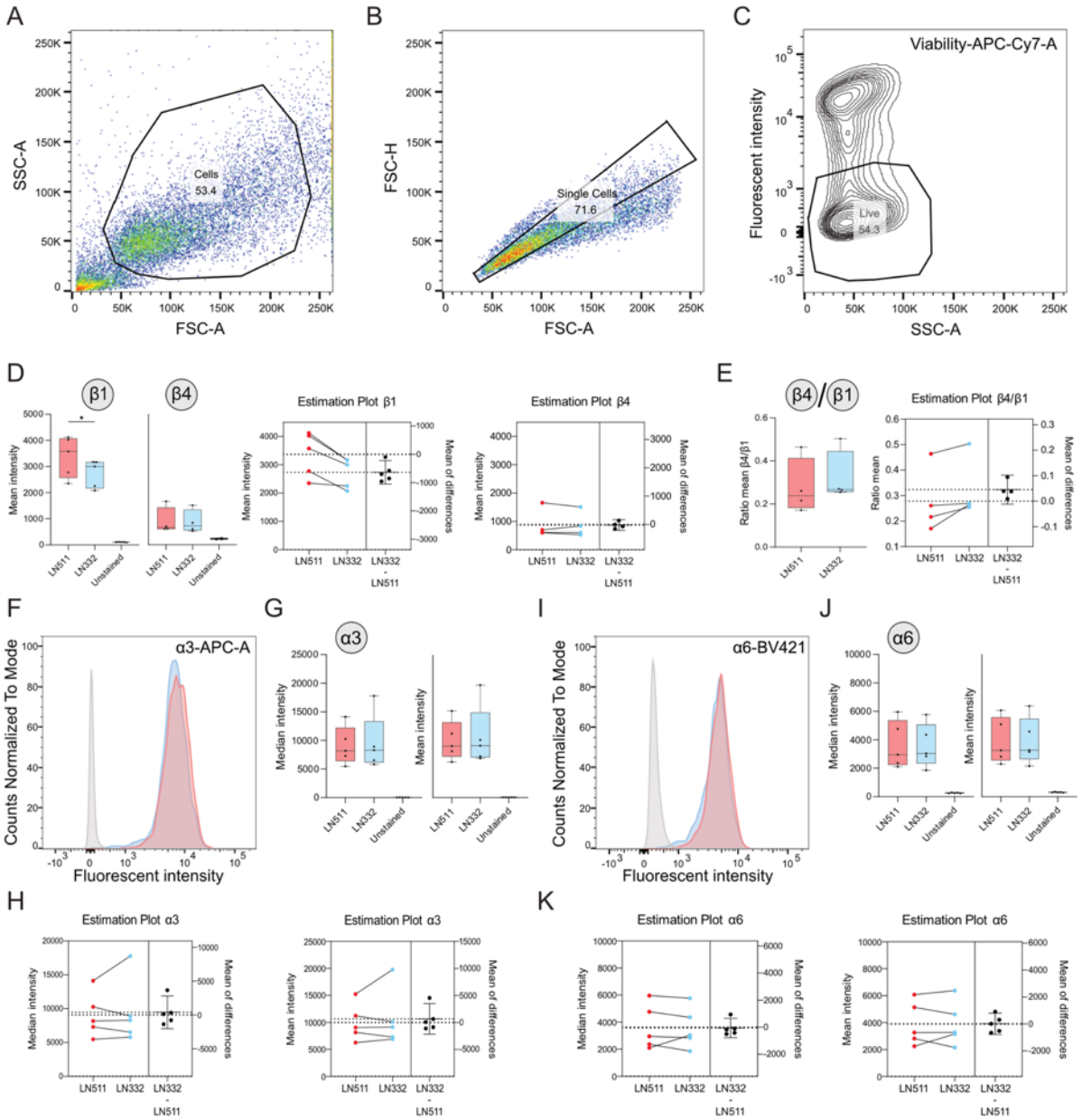

Supplementary figure 4: Flow cytometry analysis of hiPSC-RPE cultured on polyacrylamide gels coated with 5 µg/ml of laminin 511 or laminin 332. Representative dot plots showing the gating strategy to identify cells **(A)**, single cells **(B)**, contour plot to extract a population of single living cells **(C)** and gating strategy for β4-positive cells **(D)**. **(E)** Box and whisker plots of the mean intensity of integrin β1 and integrin β4 staining (left) and corresponding estimation plots (right) acquired from flow cytometry data. **(F)** Box and whisker (left) and estimation (right) plots showing the ratio between mean intensity of integrin β4 and integrin β1 staining. Representative histograms of flow cytometry analysis, box and whisker plots of median and mean fluorescent intensity and corresponding estimation plots of staining for APC-A-conjugated integrin α3 **(G, H and I)** and BV421-conjugated integrin α6 **(J, K and L)**. The grey-coloured histogram represents the signal from unstained cells. Statistical analysis was done using a paired t-test to compare results between laminin 511 and laminin 332 coatings.

785 *Table 1: List of antibodies used in this work.*

Name	Origin	Source	Concentration (µg/ml) / Dilution
Primary antibodies			
Anti mouse laminin 111 (pan-Laminin)	rabbit	Gift from Lydia Sorokin	Rabbit serum, 1:2000
Anti mouse laminin α1 (clone 200)	rat	Gift from Lydia Sorokin	Hybridoma supernatant
Anti mouse laminin α2 (clone 4H8-2)	rat	Gift from Lydia Sorokin	Hybridoma supernatant
Anti human laminin 332	rabbit	Gift from Monique Aumailley	Rabbit serum, 1:2000
Anti mouse laminin α4	rabbit	Gift from Lydia Sorokin	Rabbit serum, 1:1000
Anti mouse laminin α5	rabbit	Gift from Lydia Sorokin	Rabbit serum, 1:1000
Anti mouse collagen type IV	mouse	Merck Millipore, AB756P	12.5
Anti mouse collagen type I	rabbit	Novusbio, NB600-408	5
Anti mouse elastin	rabbit	Abcam, ab21610	5
Phalloidin iFluor 647		Abcam, ab176753	1x
Phalloidin iFluor 488		Abcam, ab176759	1x
Ant human ZO-1	rabbit	Thermo Fisher, 61-7300	5
Anti human ezrin (clone 3C12)	mouse	Abcam, ab4069	20
Anti human fibronectin	rabbit	Sigma, F3648	2.5
Antibodies used for flow cytometry			
Integrin β1-PE (clone 12G10)	mouse	Santa Cruz, sc-59827 PE	1 mg per million cells
Integrin β4-Alexa Flour 488 (clone A9)	mouse	Santa Cruz, sc-13543 AF488	1 mg per million cells
Integrin α3-Alexa Flour 647 (clone P1B5)	mouse	Santa Cruz, sc-13545 AF647	1 mg per million cells
Integrin α6-Brilliant Violet 421 (clone GOH3)	rat	BioLegend, 313623	5 ml per million cells
Secondary antibodies			
Anti-mouse-IgG AF488	goat	Invitrogen, A11001	4
Anti-mouse-IgG AF594	goat	Invitrogen, A11005	4
Anti-mouse-IgG AF647	goat	Jackson/Dianova, 111-605-144	10
Anti-rabbit-IgG AF594	goat	Invitrogen, A11012	4
Anti-rabbit-IgG AF647	goat	Molecular Probes, A21235	10
Anti-rat-IgG AF555	goat	Invitrogen, A21434	4
Anti-rat-IgG AF647	goat	Thermo Fisher, A21247	10

786
787
788 ***Table 2: Number of cells in vitro analysed for morphometric and topological parameters.***

	Laminin 322			Laminin 511		
	Exp 1	Exp 2	Exp 3	Exp 1	Exp 2	Exp 3
5 µg/mL	440 (454)	638 (654)	715 (736)	606 (625)	686 (710)	727 (753)
10 µg/mL	479 (495)	697 (719)	654 (679)	547 (561)	575 (594)	396 (415)
20 µg/mL	627 (641)	683 (698)	608 (634)	559 (572)	831 (856)	480 (499)
30 µg/mL	529 (539)	325 (334)	637 (660)	513 (525)	710 (737)	759 (782)

789
790

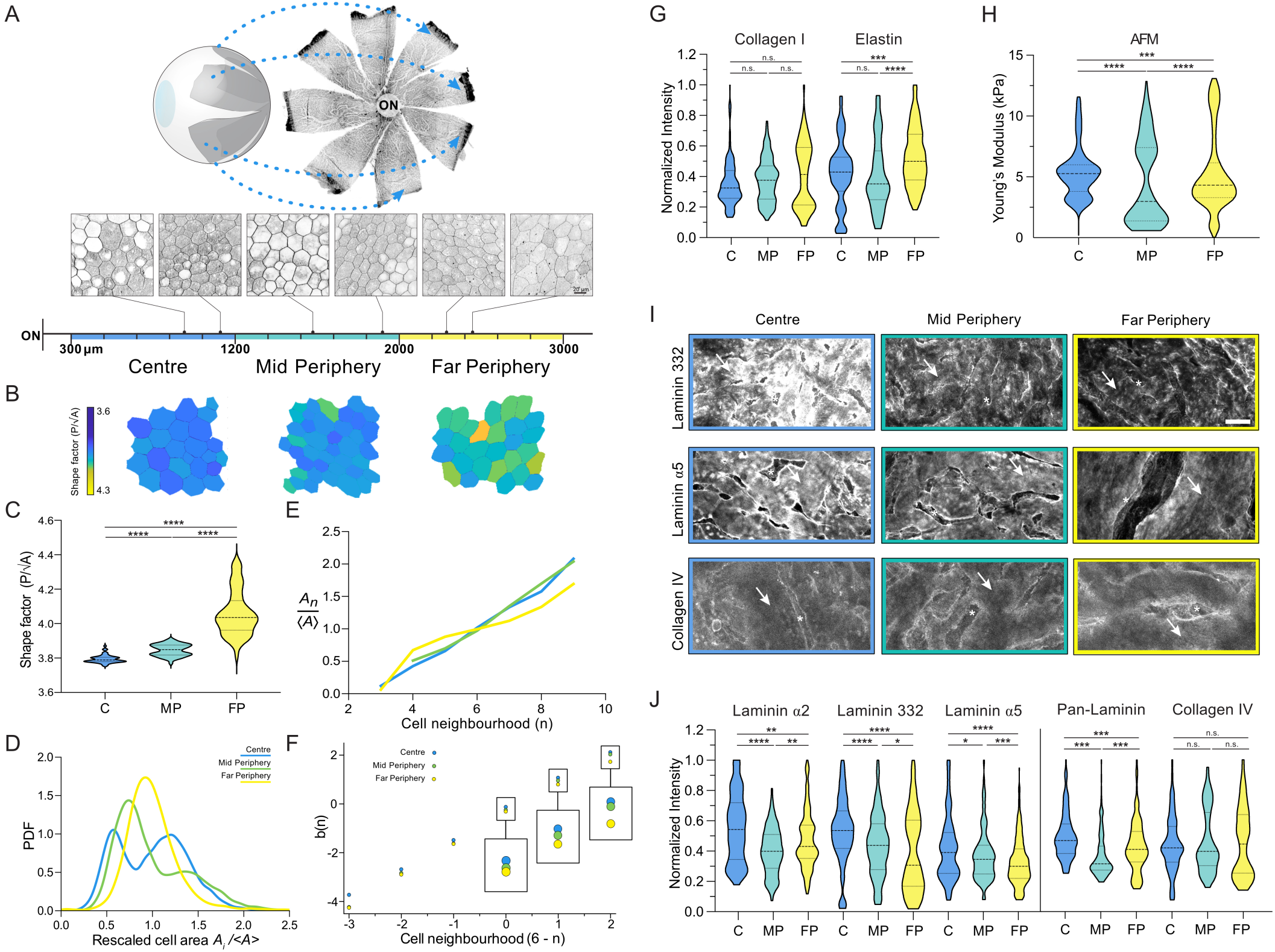
A
ON
ON
300 µm
1200
2000
3000
Centre
Mid Periphery
Far Periphery
B
Shape factor (P/√A)
3.6
4.3
C
Shape factor (P/√A)
C
MP
FP
D
PDF
Rescaled cell area A_i /<A>
Centre
Mid Periphery
Far Periphery
E
$\frac{A_n}{\langle A \rangle}$
Cell neighbourhood (n)
F
b(n)
Cell neighbourhood (6 - n)
Centre
Mid Periphery
Far Periphery
G
Collagen I
Elastin
Normalized Intensity
n.s.
***
****
H
AFM
Young's Modulus (kPa)
I
Centre
Mid Periphery
Far Periphery
Laminin 332
Laminin α5
Collagen IV
J
Laminin α2
Laminin 332
Laminin α5
Pan-Laminin
Collagen IV
Normalized Intensity

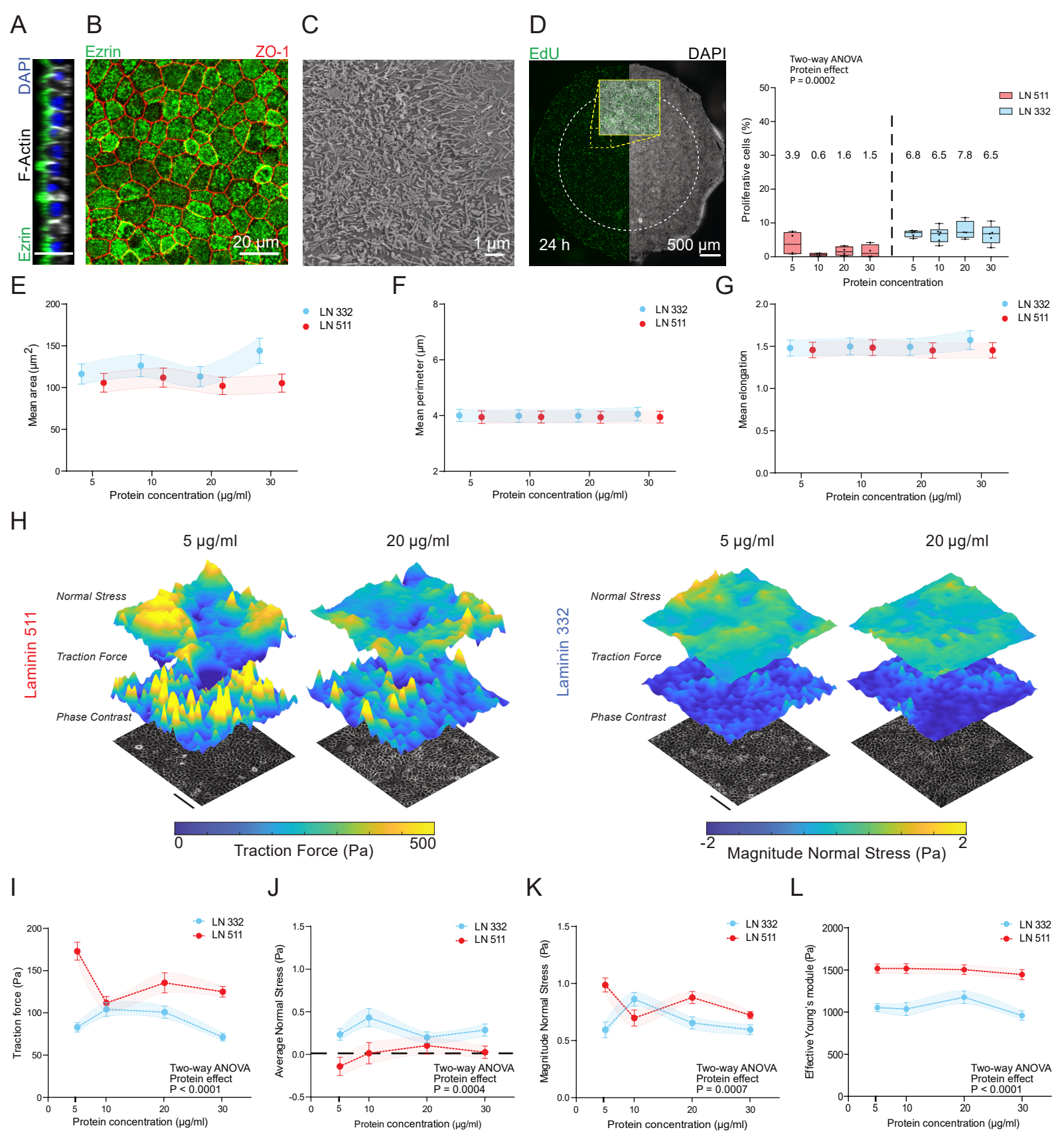
A
B
C
D
DAPI
F-Actin
Ezrin
Ezrin
ZO-1
20 µm
1 µm
EdU
DAPI
24 h
500 µm
Two-way ANOVA
Protein effect
P = 0.0002
LN 511
LN 332
Proliferative cells (%)
3.9 0.6 1.6 1.5
6.8 6.5 7.8 6.5
Protein concentration
E
Mean area (µm²)
Protein concentration (µg/ml)
F
Mean perimeter (µm)
G
Mean elongation
H
5 µg/ml
20 µg/ml
Laminin 511
Laminin 332
Normal Stress
Traction Force
Phase Contrast
0
500
Traction Force (Pa)
-2
2
Magnitude Normal Stress (Pa)
I
Traction force (Pa)
Two-way ANOVA
Protein effect
P < 0.0001
J
Average Normal Stress (Pa)
Two-way ANOVA
Protein effect
P = 0.0004
K
Magnitude Normal Stress (Pa)
Two-way ANOVA
Protein effect
P = 0.0007
L
Effective Young's module (Pa)
Two-way ANOVA
Protein effect
P < 0.0001

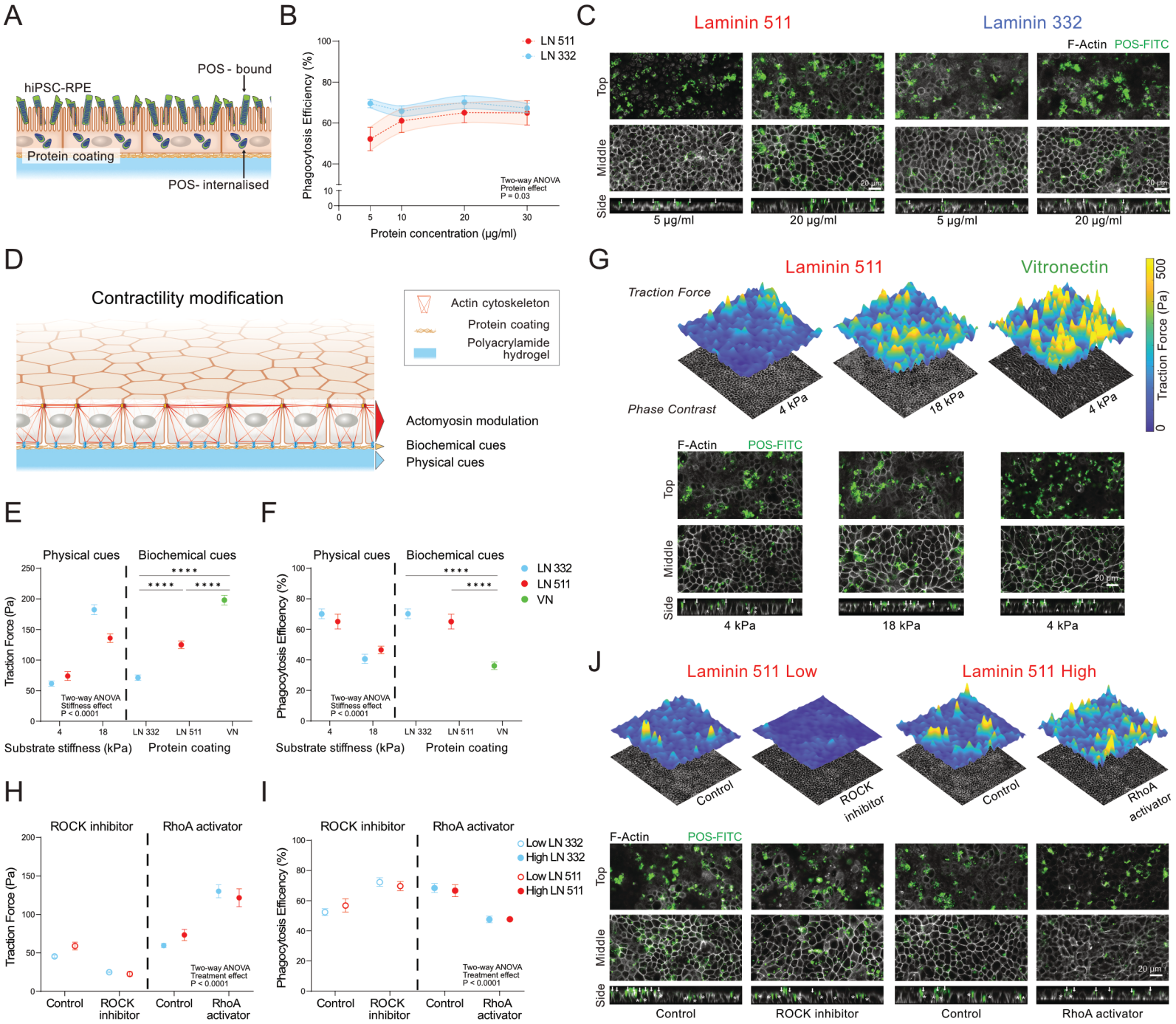
A
hiPSC-RPE
POS - bound
Protein coating
POS- internalised
B
LN 511
LN 332
Phagocytosis Efficiency (%)
Protein concentration (µg/ml)
Two-way ANOVA
Protein effect
P = 0.03
C
Laminin 511
Laminin 332
F-Actin POS-FITC
Top
Middle
Side
5 µg/ml
20 µg/ml
5 µg/ml
20 µg/ml
D
Contractility modification
Actin cytoskeleton
Protein coating
Polyacrylamide hydrogel
Actomyosin modulation
Biochemical cues
Physical cues
E
Physical cues
Biochemical cues
Traction Force (Pa)
Two-way ANOVA
Stiffness effect
P < 0.0001
Substrate stiffness (kPa)
Protein coating
F
Physical cues
Biochemical cues
LN 332
LN 511
VN
Phagocytosis Efficency (%)
Two-way ANOVA
Stiffness effect
P < 0.0001
Substrate stiffness (kPa)
Protein coating
G
Laminin 511
Vitronectin
Traction Force
Phase Contrast
4 kPa
18 kPa
4 kPa
Traction Force (Pa)
F-Actin POS-FITC
Top
Middle
Side
4 kPa
18 kPa
4 kPa
H
ROCK inhibitor
RhoA activator
Traction Force (Pa)
Two-way ANOVA
Treatment effect
P < 0.0001
Control
ROCK inhibitor
Control
RhoA activator
I
ROCK inhibitor
RhoA activator
Low LN 332
High LN 332
Low LN 511
High LN 511
Phagocytosis Efficency (%)
Two-way ANOVA
Treatment effect
P < 0.0001
Control
ROCK inhibitor
Control
RhoA activator
J
Laminin 511 Low
Laminin 511 High
Control
ROCK inhibitor
Control
RhoA activator
F-Actin POS-FITC
Top
Middle
Side
Control
ROCK inhibitor
Control
RhoA activator

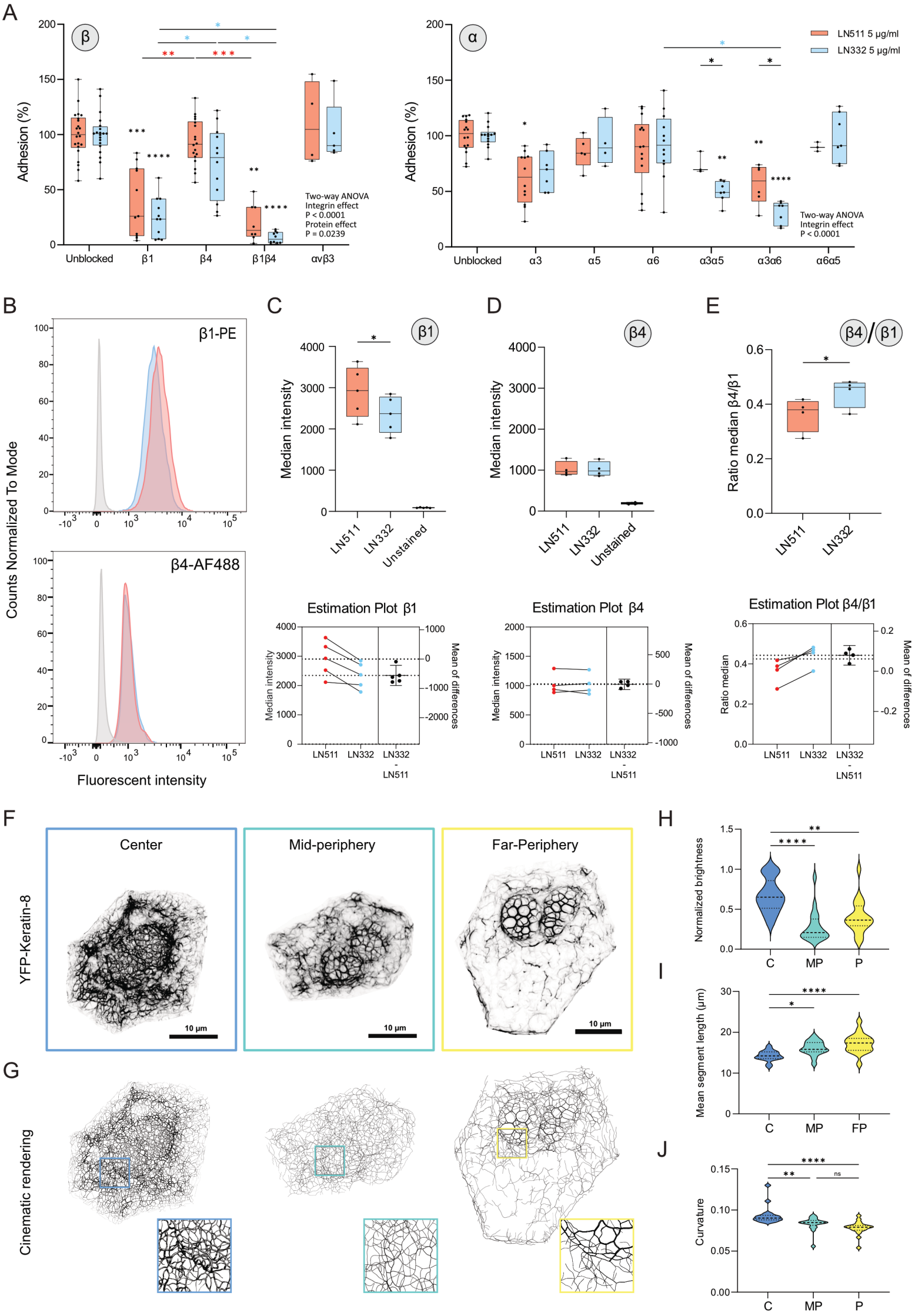
A
β
Adhesion (%)
Unblocked
β1
β4
β1β4
αvβ3
Two-way ANOVA
Integrin effect
P < 0.0001
Protein effect
P = 0.0239
α
LN511 5 µg/ml
LN332 5 µg/ml
α3
α5
α6
α3α5
α3α6
α6α5
Two-way ANOVA
Integrin effect
P < 0.0001
B
β1-PE
β4-AF488
Counts Normalized To Mode
Fluorescent intensity
C
β1
Median intensity
LN511
LN332
Unstained
Estimation Plot β1
Mean of differences
D
β4
Estimation Plot β4
E
β4/β1
Ratio median β4/β1
Estimation Plot β4/β1
Ratio median
F
Center
Mid-periphery
Far-Periphery
YFP-Keratin-8
10 µm
G
Cinematic rendering
H
Normalized brightness
C
MP
P
I
Mean segment length (µm)
FP
J
Curvature
ns

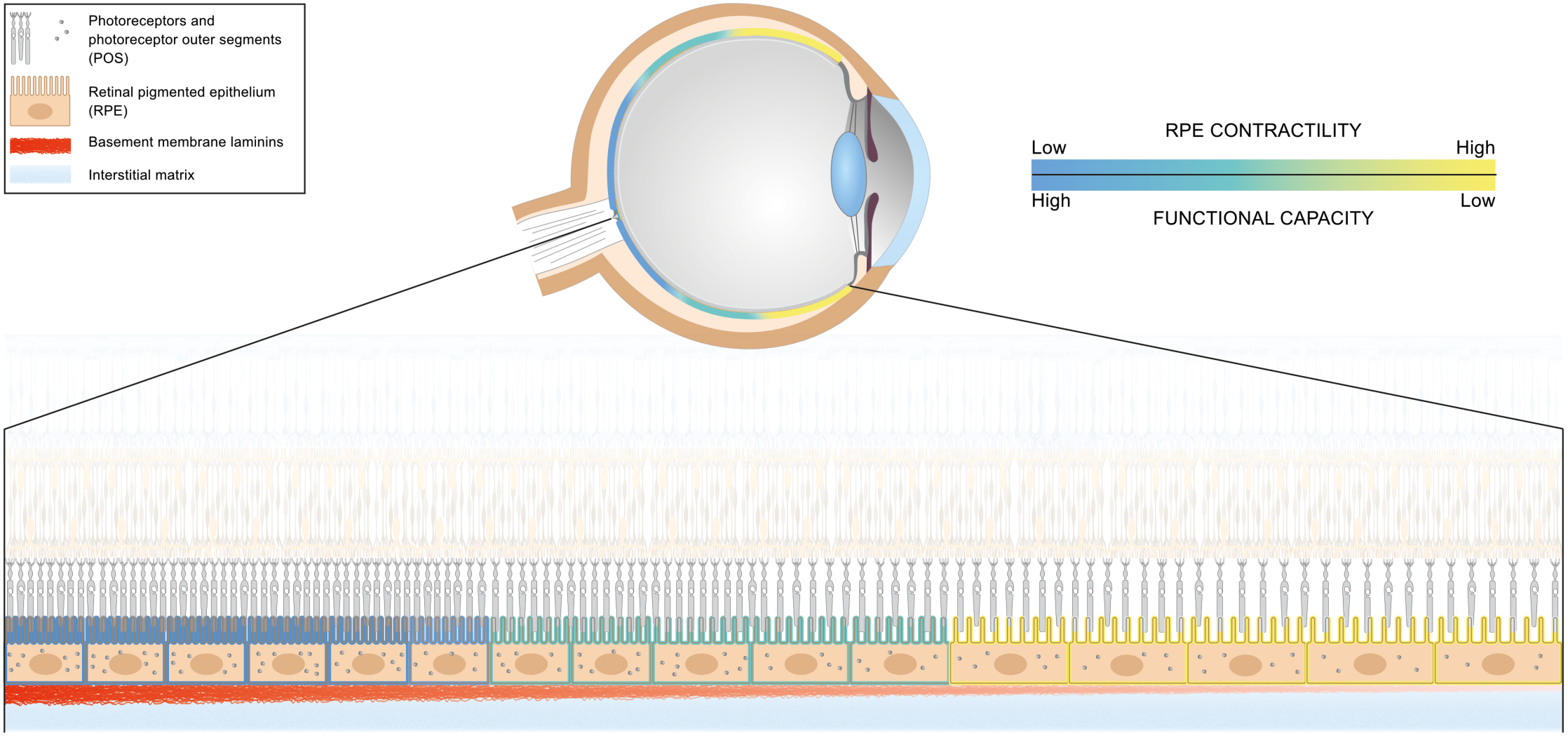
Photoreceptors and photoreceptor outer segments (POS)
Retinal pigmented epithelium (RPE)
Basement membrane laminins
Interstitial matrix
RPE CONTRACTILITY
Low
High
High
Low
FUNCTIONAL CAPACITY